Nano Research

ISSN 1998-0124 CN 11-5974/O4
https://doi.org/10.26599/NR.2026.94908873

Research Article

# Exact charge transfer control in quantum dots/molecule system–induced large emission contrast for ultrasensitive and anti-interfering detection

Rongchao Zhu[1,2], Zhenzhen Cai[1](✉), Xu Cheng[1,2], Luyan Yang[1], Baiyi Zu[1], Xincun Dou[1,2](✉)

[1] Xinjiang Key Laboratory of Trace Chemical Substances Sensing, Xinjiang Technical Institute of Physics and Chemistry, Chinese Academy of Sciences, Urumqi 830011, China

[2] Center of Materials Science and Optoelectronics Engineering, University of Chinese Academy of Sciences, Beijing 100049, China

*Nano Res.*, **Just Accepted Manuscript** • https://doi.org/10.26599/NR.2026.94908873

**https://www.sciopen.com/journal/1998-0124** on May. 25, 2026



## Just Accepted

## TABLE OF CONTENTS (TOC)

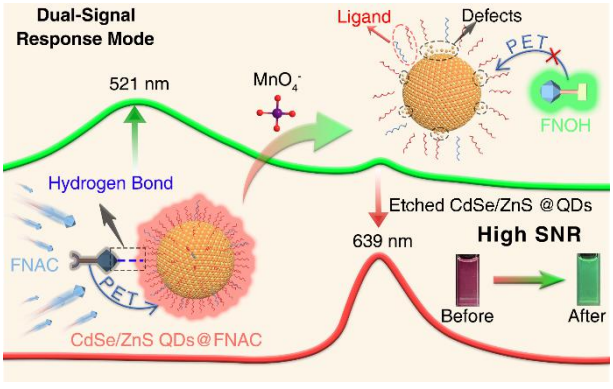


A hydrogen bond-driven non-covalent self-assembled CdSe/ZnS QDs@FNAC system, composed of carboxyl-terminated quantum dots (CdSe/ZnS QDs@MPA) and a naphthol-based molecular probe (FNAC), was rationally designed. This system enables a ratiometric fluorescent dual-signal response toward $KMnO_4$ based on the synergistic mechanism of PET and TICT, featuring excellent sensing performance including a fast response speed (1 s), high sensitivity (4.80 nM), a favorable SNR, and negligible interference from other oxidants.

Research Article

# Exact charge transfer control in quantum dots/molecule system–induced large emission contrast for ultrasensitive and anti-interfering detection

Rongchao Zhu[1,2], Zhenzhen Cai[1,✉], Xu Cheng[1,2], Luyan Yang[1], Baiyi Zu[1], and Xincun Dou[1,2,✉]

[1] *Xinjiang Key Laboratory of Trace Chemical Substances Sensing, Xinjiang Technical Institute of Physics and Chemistry, Chinese Academy of Sciences, Urumqi 830011, China*
[2] *Center of Materials Science and Optoelectronics Engineering, University of Chinese Academy of Sciences, Beijing 100049, China*

**Received:** 8 April 2026; **Revised:** 20 May 2026; **Accepted:** 25 May 2026

✉ Address correspondence to Zhenzhen Cai, caizz@ms.xjb.ac.cn; Xincun Dou, xcdou@ms.xjb.ac.cn

**Cite this article:** *Nano Research*, 2026, 19, 9490886773 https://doi.org/10.26599/NR.2026.94908873

**ABSTRACT:** The design of unique fluorescent probes is of paramount importance for boosting the signal-to-noise ratio (SNR) and improving the sensitivity toward target analytes. Herein, we report a hydrogen-bond-driven self-assembled sensing system (CdSe/ZnS QDs@FNAC) composed of quantum dots capped with 3-mercaptopropionic acid (CdSe/ZnS QDs@MPA) and a naphthol-based molecular probe (FNAC) that enables the precise modulation of photoinduced electron transfer (PET) and twisted intramolecular charge transfer (TICT) processes. The surface carboxyl groups on CdSe/ZnS QDs@MPA facilitate FNAC anchoring through hydrogen bonding, ensure water solubility, and generate a localized acidic microenvironment to enhance the oxidative reactivity of potassium permanganate ($KMnO_4$). Upon exposure to $KMnO_4$, the PET process of CdSe/ZnS QDs@FNAC was disrupted, triggering oxidative etching–induced fluorescence quenching of the CdSe/ZnS QDs and suppressing the TICT process of the released FNAC probe, resulting in a distinct green fluorescence turn-on response. The ratiometric fluorescence system with a dual-signal response mode enabled the detection of $KMnO_4$ with rapid response (1 s), high sensitivity (4.80 nM), and excellent SNR, while interference from other oxidants was negligible. The practicality of CdSe/ZnS QDs@FNAC was further verified by integrating a CdSe/ZnS QDs@FNAC-embedded hydrogel-based sensing chip into a portable detector, which enabled the on-site identification of ng-level $KMnO_4$ particles with high selectivity.

**KEYWORDS:** semiconductor quantum dots, potassium permanganate, ratiometric fluorescence sensing, dual-signal response, hydrogel-based sensor



## 1 Introduction

Optical chemical sensing effectively transduces chemical information [1, 2] such as the qualification or quantitation of a target analyte [3, 4] into measurable optical signals *via* photophysical or photochemical processes [5, 6]. Owing to its high sensitivity, this approach has broad applications in diverse fields, including medical diagnostics [7, 8], industrial process control [7, 9], intelligent environmental monitoring [10], and trace substance detection [3, 11]. Generally, interactions between sensing materials and analytes can induce detectable changes in optical parameters, including emission intensity [12, 13], wavelength [14, 15], phase [16, 17], and polarization [18, 19], with measurable signals for quantitative analysis. Unlike conventional sensing strategies that rely solely on signal intensity changes, ratiometric fluorescence sensing employs an internal self-referencing mechanism in which the ratio of the fluorescence intensities at two distinct wavelengths ($R=R_1/R_2$) serves as the analytical output [13, 20]. This self-referencing mode provides a more reliable sensing parameter that directly correlates with the analyte concentration and offers distinct advantages, including high signal-to-noise ratio (SNR) [21, 22], robust immunity to interference [21, 23], excellent accuracy [23, 24], and enhanced photostability [25, 26]. Generally, ratiometric fluorescent sensors are categorized according to their signal response behavior upon interaction with target analytes [27, 28]. Single-signal sensors exhibit variations in only one fluorescence channel [10], whereas dual-signal sensors exhibit concurrent or independent changes in two distinct emission signals [29]. In the ideal dual-signal response mode, an increase in one signal is accompanied by a decrease in the other, leading to a substantially larger change in the fluorescence intensity ratio (R) than the absolute variation in either signal alone [29]. This intrinsic signal amplification can effectively compensate for the fluctuations arising from the probe concentration, instrumental instability, and environmental factors, markedly enhancing the detection sensitivity and SNR and enabling reliable detection of trace-level analytes [27, 30, 31]. Consequently, the construction of an ideal dual-signal-responsive ratiometric system with mutually opposing signal changes is of great importance, prompting the exploration of advanced luminescent nanomaterials capable of integrating dual-emission behavior with analyte-triggered synergistic responses.

Semiconductor quantum dots (QDs) have emerged as ideal candidates for achieving such high-performance sensing platforms owing to their size-tunable emission wavelengths, broad excitation spectra, narrow emission bands, high quantum yields, and exceptional photostability [32–34]. QDs and their hybrid materials have been widely employed in fluorescent sensing and have become mainstream nanoprobes, primarily for the detection of ions[35, 36] and biomarkers [37, 38]. To date, reported sensing systems based on semiconductor QDs have predominantly relied on a single-signal response mode, which

can be broadly classified into

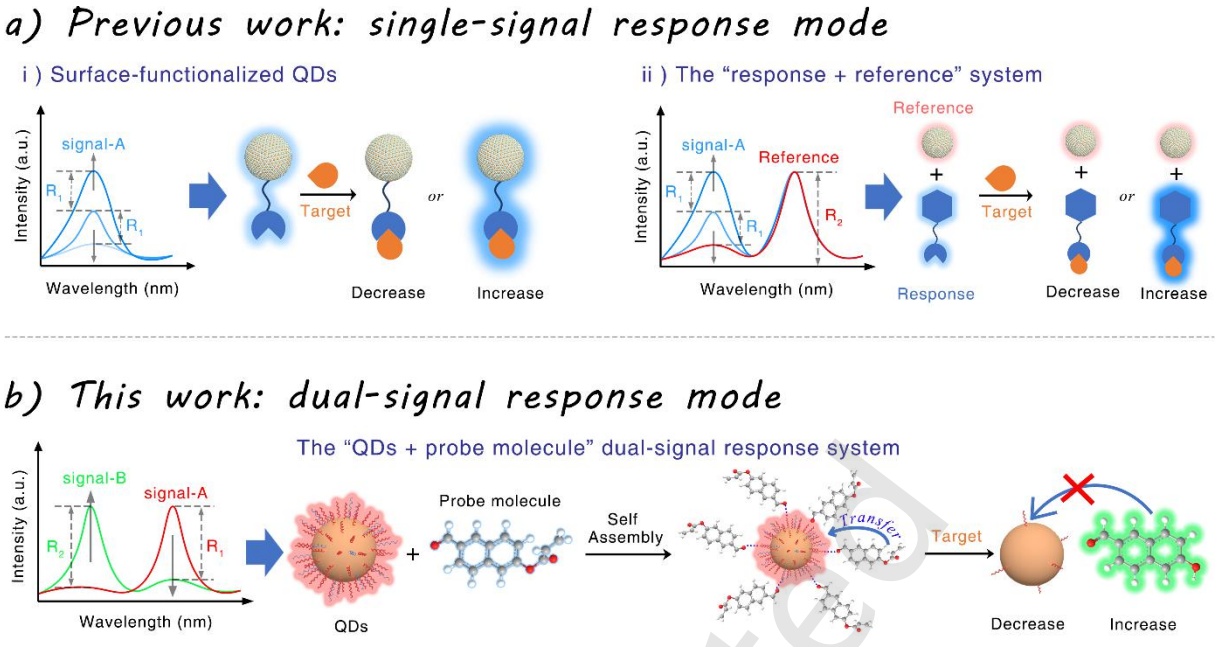


**Scheme 1.** (a) Schematic illustrations of conventional QDs-based fluorescence sensing strategies relying on a single-signal response: (i) pristine or surface-functionalized QDs and (ii) "responsive + reference" QDs-based hybrid system. (b) The design strategy and reaction mechanism of the self-assembled "QDs + probe molecule" system developed herein for dual-signal responses towards target analytes.

two categories: (i) pristine [39, 40] or surface-functionalized QDs [41, 42] (**Scheme 1**ai), and (ii) "responsive + reference" dual-fluorophore systems [34, 43] (Scheme 1aii). Pristine or surface-functionalized QDs in the first category typically operate in a single-signal response mode, wherein analyte-induced fluorescence modulations, such as quenching or enhancement, are primarily driven by Förster resonance energy transfer (FRET) [39, 44] or surface etching [45]. The second category, which represents the mainstream approach, employs QDs as inert reference standards paired with responsive elements to achieve self-calibrating ratiometric detection, a process predominantly driven by FRET [46, 47], or the inner filter effect [48, 49]. Consequently, both categories exhibit an inherent limitation: signal modulation is confined to a single fluorophore, which restricts the dynamic range of the ratiometric output. By contrast, employing a synergistic dual-signal response mode, wherein analyte interactions trigger simultaneous and opposing changes in both emission channels, effectively circumvents this restriction. However, realizing such synchronized signal reversal is scientifically challenging, as it requires the precise regulation of the intermolecular charge transfer to strictly dictate the "ON/OFF" states of both components within a single integrated assembly. Conventional construction strategies often lack the structural precision required to rigorously control the electronic interactions at the interface, creating a barrier to engineering high-performance sensors with such dual-signal response modes. Therefore, constructing a robust sensing platform by designing structural complementarities between the surface ligands of semiconductor QDs and organic dyes is necessary, facilitating the development of QDs-based materials with ratiometric dual-signal fluorescence responses.

Herein, we propose a hydrogen-bond-driven self-assembly strategy to construct a "QDs + probe molecule" system, in which FNAC is precisely anchored onto the surface of carboxyl (–COOH)-terminated CdSe/ZnS QDs@3-mercaptopropionic acid (MPA) via hydrogen bonding (Scheme 1b). To verify the dual-signal response mode of this self-assembled system, $KMnO_4$, a representative raw material for producing improvised explosives, was selected as the target analyte for qualitative analysis. Specifically, the –COOH groups on the surface of the QDs played a critical role in enhancing the oxidizing ability of $KMnO_4$ during its interaction with the probe FNAC. Upon exposure to $KMnO_4$, the QDs undergo oxidative etching accompanied by fluorescence quenching, whereas the surface-anchored acrylate-bearing probes are oxidatively cleaved and then hydrolyzed, liberating fluorophores that emit a distinct green fluorescence signal. Moreover, a CdSe/ZnS QDs@FNAC-embedded hydrogel-based sensing chip was fabricated, and its practicality was verified by integrating it into a portable detector, enabling the specific and qualitative detection of $KMnO_4$ particles in practical scenarios.

## 2 Experimental

### 2.1 Synthesis of the FNAC

6-Hydroxy-2-naphthaldehyde (1 mmol, 172 mg), triethylamine ($Et_3N$, 2.25 mmol, 228 mg), and dichloromethane (DCM) (20 mL) were mixed thoroughly in a 100 mL triple-necked flask equipped with a magnetic stir bar and chilled in an ice bath. Subsequently, acryloyl chloride (1.5 mmol, 136 mg) was added dropwise to the chilled mixture under stirring. The reaction mixture was stirred at 0 °C for 30 min and then at room temperature for 12 h. The resulting mixture was diluted with DCM (30 mL). The organic layer was then separated, washed sequentially with deionized water (15 mL × 3), and dried over anhydrous $Na_2SO_4$. The crude product was purified by silica gel column chromatography using petroleum ether/ethyl acetate (5:1, v/v, $R_f$ = 0.5) as the eluent.

### 2.2 Synthesis of the CdSe/ZnS QDs@OA

The CdSe/ZnS core/shell QDs used in this study were synthesized via the hot injection method, following the synthetic

rationale described in a previous report, with minor modifications [50]. Briefly, 1 mmol of CdO, 1.68 mmol of $ZnAc_2$, and 5 mL of oleic acid (OA) were added to a 50 mL three-necked flask and heated to 140 °C under a nitrogen ($N_2$) flow for 30 min. After cooling the solution to 50 °C, 25 mL of 1-ODE was added, and the mixture was heated to 300 °C under continuous $N_2$ protection. Separately, injection solutions of 1 M trioctylphosphine-selenium (TOP-Se) solution and 2 M trioctylphosphine-sulfur (TOP-S) solution were prepared by stirring at 800 rpm at 100 °C until complete dissolution. At 300 °C, 0.2 mL of the TOP-Se solution was rapidly injected into the reaction flask and kept for 80 s. Next, 0.3 mL of 1-DDT dissolved in 1 mL of 1-ODE was injected into the system, and the reaction continued for 20 min. Subsequently, 1 mL of the TOP-S solution was slowly injected into the flask over 10 min. Finally, the reaction mixture was cooled to room temperature to yield OA-capped CdSe/ZnS QDs (CdSe/ZnS QDs@OA) with red emission.

The as-prepared CdSe/ZnS QDs@OA were purified via a precipitation-redispersion method [51] using a DCM/MeOH solvent system with a volume ratio of 1:1. This purification procedure was repeated five times. Subsequently, the purified CdSe/ZnS QDs@OA were dried, stored at -20 °C, and reserved for subsequent experiments.

### 2.3 Synthesis of the CdSe/ZnS QDs@MPA

The CdSe/ZnS QDs capped with MPA (denoted as CdSe/ZnS QDs@MPA) were obtained from a previous report [52]. Briefly, 0.2 g of oleic acid–capped CdSe/ZnS QDs (CdSe/ZnS QDs@OA) and methanol (15 mL) were added to a 100 mL three-necked flask. Subsequently, tetramethylammonium hydroxide solution (25%) was slowly added dropwise to adjust the pH of the mixture to 10, after which 5 mL of MPA was added to the flask. The resulting mixture was stirred at 800 rpm and 65 °C for 6 h until all the CdSe/ZnS QDs@MPA particles were transferred from the original phase to the methanol phase.

The as-prepared CdSe/ZnS QDs@MPA was purified via a precipitation-redispersion method using a DCM/MeOH solvent system with a volume ratio of 20:20. This purification procedure was repeated five times. Subsequently, the purified CdSe/ZnS QDs@MPA were dried, stored at -20 °C, and reserved for subsequent experiments.

### 2.4 Preparation of the CdSe/ZnS QDs@FNAC

CdSe/ZnS QDs@MPA (1.6 mg) and FNAC (2.26 mg, 10 μmol) were placed in a 200 mL flask, 100 mL of $CH_3CN/H_2O$ was added as a solvent, and the resulting mixture was reacted at room temperature for 30 min to yield the CdSe/ZnS QDs@FNAC.

### 2.5 Preparation of CdSe/ZnS QDs@FNAC-Based Polyacrylamide Hydrogel Sensing Chip.

Acrylamide (19.7 mmol, 1.4 g), 10.0 mg of *N*,*N*'-methylene diacrylamide (64.8 μmol), 9.0 mg of azobisisobutyronitrile (54.8 μmol), 1 mL of CdSe/ZnS QDs@MPA solution (0.8 mg/mL), and 9 mL of deionized water were thoroughly mixed in a 50 mL flask. The mixture was stirred at 520 rpm at room temperature for 2 h, transferred to a glass mold, and incubated at 60 °C for 3 h to initiate polymerization. The obtained polyacrylamide hydrogel was cut into 5×5 cm squares and immersed in a FNAC solution (100 μM). A CdSe/ZnS QD@FNAC-based polyacrylamide hydrogel sensor was fabricated using the solvent displacement method.

## 3 Results and discussion

### 3.1 Design Strategy of Self-Assembly-Based Dual-Signal Response Mode Ratiometric Fluorescence System CdSe/ZnS QDs@FNAC

Based on the photoinduced electron transfer (PET) mechanism, a non-fluorescent D-π-A optical probe was anchored onto the surface of CdSe/ZnS QDs@MPA *via* hydrogen-bond-driven self-assembly (**Figure 1**a). Introduced analytes can disrupt intermolecular hydrogen bonds and chemically react with both QDs and optical probes, resulting in fluorescence quenching and turn-on, respectively. This strategy is expected to realize a ratiometric fluorescence shift from red to green emission, enabling a dual-signal response mode with a high SNR and exceptional visual contrast. To investigate the reactivity and reactive sites of $KMnO_4$, its electrostatic potential (ESP) of $KMnO_4$ was calculated using the local density approximation. The resulting distribution map reveals exclusively negative ESP values (ranging from -5.95~-3.29 kcal/mol), confirming the nucleophilic character of $MnO_4^-$ (Figure 1bi). Notably, the oxidative potentials of $KMnO_4$ under acidic-to-neutral (standard electrode potential $E^o$ = +1.70 V) and strongly acidic conditions ($E^o$ = +1.51 V) are significantly higher than those under alkaline conditions ($E^o$ = +0.59 V) [53] (Figure 1bii, Scheme S1).

To simultaneously enhance the aqueous solubility and create a localized acidic microenvironment that boosts the oxidizing ability of $KMnO_4$, a ligand-exchange strategy was employed to fabricate MPA-capped CdSe/ZnS QDs, which were used as functional carriers (Scheme S2). Considering the strong oxidative capacity and nucleophilicity of $MnO_4^-$, the FNAC probe was rationally designed, featuring electron-deficient aldehyde (–CHO) and acrylate moieties to facilitate molecular assembly and serve as recognition sites (Scheme S3, Figures S1–S3). The analysis shows that the maximum ESP of FNAC is localized at the acrylate group (29.86 kcal/mol), indicating that this group serves as the preferential reaction site with $MnO_4^-$ (Figure 1biii). The –COOH groups on the surface of the CdSe/ZnS QDs@MPA further interacted with the –CHO groups in FNAC via hydrogen bonding, forming a self-assembled system denoted as CdSe/ZnS QDs@FNAC, which exhibited fluorescence emission at 639 nm under excitation at 365 nm (Figure 1c). Upon exposure to $KMnO_4$, the intermolecular hydrogen bonds between CdSe/ZnS QDs@MPA and FNAC were disrupted, and $KMnO_4$ further etched the QDs, leading to the detachment of ligands from the surface of the QDs and consequent fluorescence quenching of the QDs. Meanwhile, the unsaturated double bond of the acrylate group in FNAC was first oxidized by $KMnO_4$ to 2,3-dihydroxypropyl, which was further hydrolyzed to 6-hydroxy-2-naphthaldehyde (FNOH), inhibiting the twisted intramolecular charge transfer (TICT) process, generating green fluorescence at 521 nm (Figures S4 and S5).This dual-signal response mode not only improves the SNR for $KMnO_4$ detection but also facilitates visualization by the naked eye,.

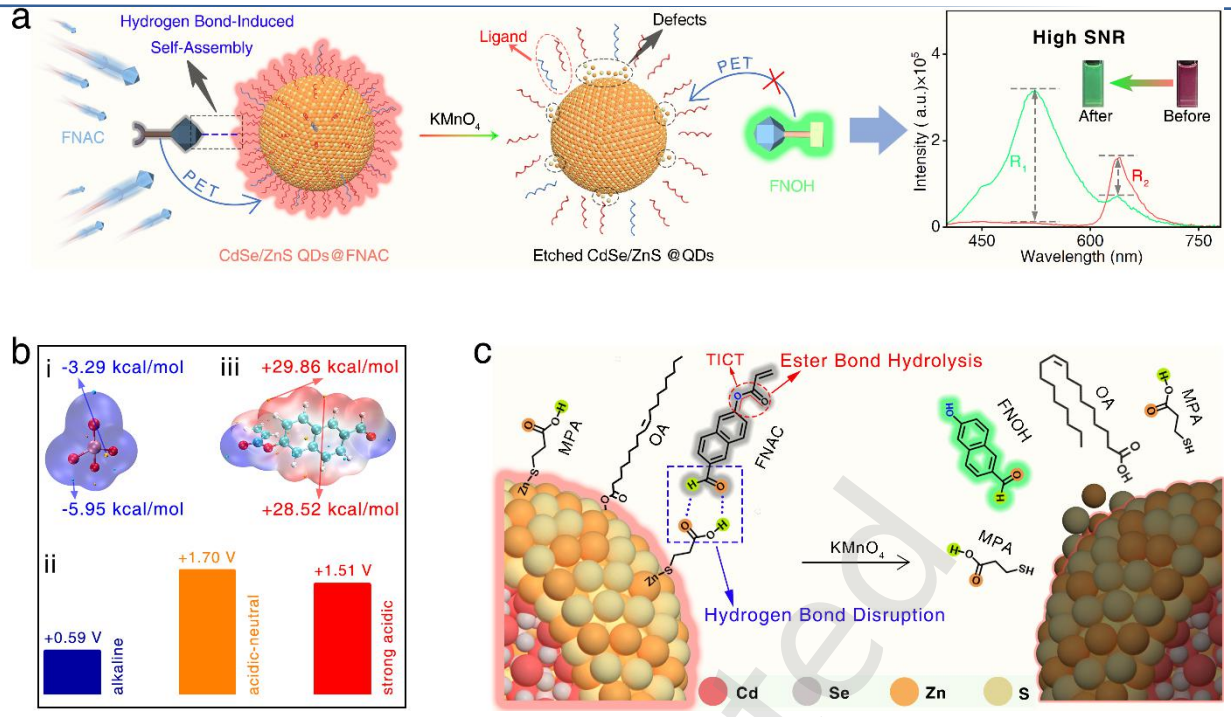


**Figure 1.** (a) The schematic illustration of the design strategy of the dual-signal response mode ratiometric fluorescence system CdSe/ZnS QDs@FNAC. (b) (i) Electrostatic potential distribution diagrams of the $KMnO_4$ and (ii) oxidative reactivity of $KMnO_4$ under different acidic and basic conditions and (iii) electrostatic potential distribution diagrams of FNAC. (c) Proposed detection mechanism of the CdSe/ZnS QDs@FNAC for $KMnO_4$ recognition.

providing a material design strategy for the on-site, high-sensitivity analysis of target analytes.

### 3.2 Construction Mechanism and Luminescent Properties of CdSe/ZnS QDs@FNAC

To clearly demonstrate the superiority of CdSe/ZnS QDs@FNAC, step-by-step characterization was systematically investigated, and the relevant optical properties and mechanisms were compared with those of their counterparts, including the FNAC and CdSe/ZnS QDs@MPA (Figure S6, Table S1). To enable an intuitive analysis of the optical behaviors of FNAC, CdSe/ZnS QDs@MPA, and CdSe/ZnS QDs@FNAC, fluorescent imaging and emission spectroscopy measurements were performed under excitation with a 365 nm UV light. Fluorescence spectrum analysis revealed that FNAC (22.70 μg/mL) and the CdSe/ZnS QDs@MPA (16.00 μg/mL) exhibited emission peaks at 449 nm and 639 nm, respectively, whereas the CdSe/ZnS QDs@FNAC (38.70 μg/mL) displayed dual emission peaks at 447 nm and 639 nm (**Figure 2**a-2c). The formation of the self-assembled CdSe/ZnS QDs@FNAC induced a slight blue shift in both emission channels, accompanied by an approximately 10% decrease in the emission intensity of FNAC, indicating the presence of specific intermolecular interactions between FNAC and CdSe/ZnS QDs@MPA.

To further investigate the intrinsic molecular origin underlying the characteristic fluorescence behavior of the optical probe FNAC, the dihedral angle between the acrylate ester group and the naphthalene moiety was systematically analyzed (Figure 2d). The potential energy surface curve clearly demonstrates that as the dihedral angle rotates from 0° to 87.55° without a barrier, the energy of the singlet ground state ($S_0$) gradually increases from the minimum to the maximum value (Figure 2e). At the dihedral angle of 0°, the electronic excitation from $S_0$ to the first singlet excited state ($S_1$) is dominated by a vertical transition, yielding an oscillator strength (*f*) of 0.4020 and a vertical excitation energy of 3.61 eV. According to Kasha's rule, the excited electrons state subsequently undergoes a rapid non-radiative relaxation to the lowest vibrational level of the $S_1$ state. Upon twisting to a dihedral angle of 77.55°, the $S_1$ state reached its energetic minimum, in which the vertical electronic emission to the $S_0$ state dominated the fluorescence behavior, with a vertical emission energy of 3.39 eV and *f* of 0.0027, indicating that the fluorescence emission of the optical probe FNAC was quenched by the twisted intramolecular charge transfer (TICT) effect. Dividing FNAC into four fragments, holes (x-axis) and electrons (y-axis) in the fragment charge transfer density matrix heatmap are primarily distributed in fragments 2 (red region) and 3 (green region) respectively, indicating that the excited state of FNAC is essentially a π-π* localized excitation confined to the naphthalene ring (Figure 2f). When the dihedral angle deviates from 0°, the conjugated plane is disrupted, and the excitons localized on the naphthalene ring are forced to transfer to the acrylate group, thereby triggering the TICT process. Furthermore, the independent gradient model (IGM) analysis revealed the presence of strong noncovalent interactions (blue region) between the CdSe/ZnS QDs@MPA and FNAC, which were caused by hydrogen bonding between the -COOH groups of the CdSe/ZnS QDs@MPA and the -CHO groups of FNAC (Figure 2g). The discrete points in the scatter plots of the two clusters exhibit a similar pattern, with spikes occurring around the negative sign ($\lambda_2$) ρ (−0.117) and a high δ value (0.113), signifying strong attractive interactions and confirming the formation of a hydrogen-bond-driven self-assembled system.

Fourier-transform infrared analysis demonstrated that upon the introduction of the optical probe FNAC into CdSe/ZnS QDs@MPA, sharp stretching vibration peaks attributed to –C=O and –C–(C=O)–O– appeared at 1732 $cm^{-1}$ and 1147 $cm^{-1}$, respectively (Figure 2h). Furthermore, the

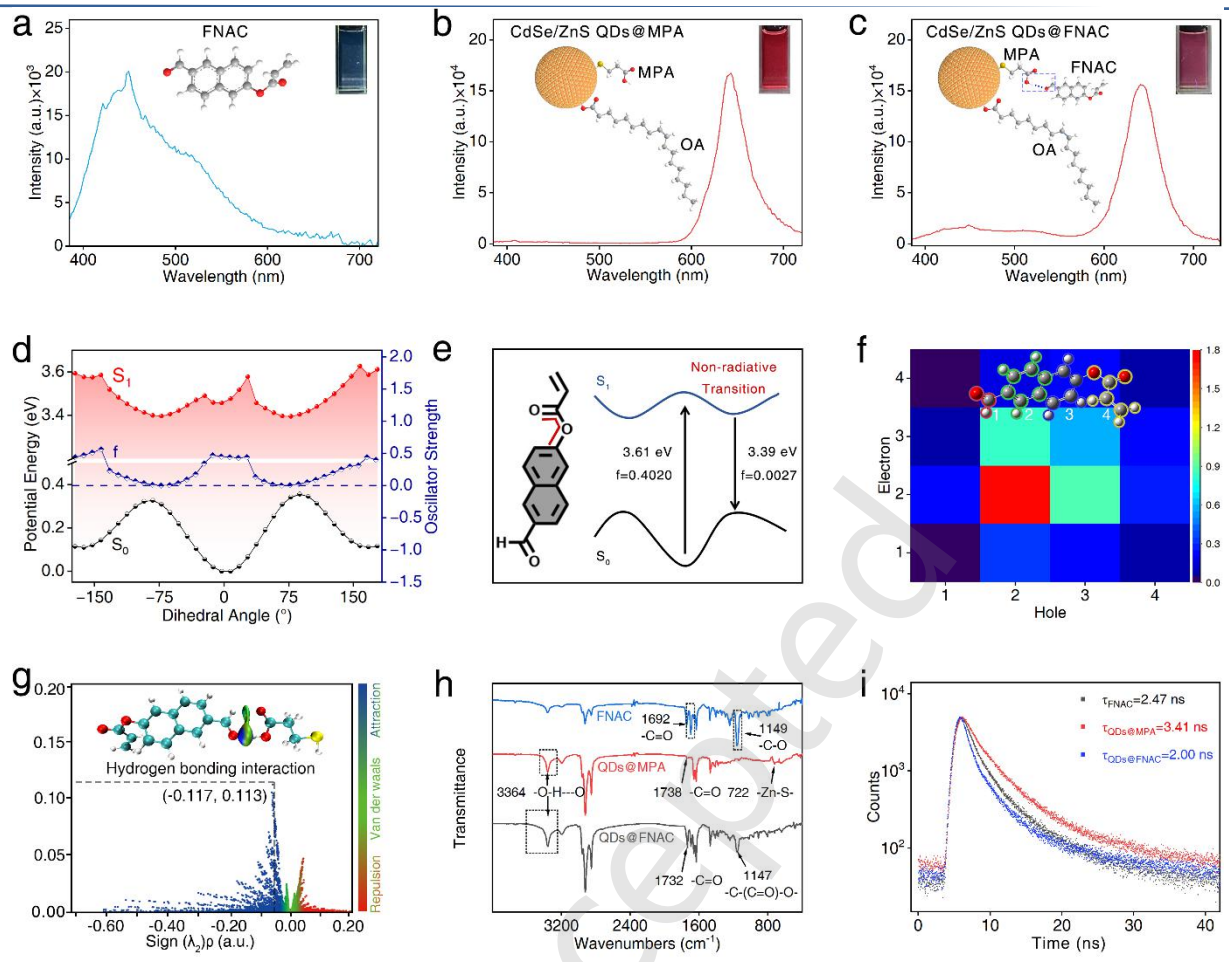


**Figure 2.** Structural diagrams, fluorescence emission spectra, and corresponding optical images of (a) FNAC, (b) CdSe/ZnS QDs@MPA, and (c) CdSe/ZnS QDs@FNAC under 365 nm UV excitation. (d) The potential energy surfaces of the $S_1$ and $S_0$ states of FNAC, and the oscillator strength (*f*) of the $S_1$ to $S_0$ transition versus the dihedral angle between the acryloyl group and the naphthalene ring. (e) The energy potential surface of the probe molecule FNAC and the corresponding dihedral angle, vertical excitation, and vertical emission. (f) The fragment transition density matrix maps of FNAC. (g) Noncovalent interaction isosurface (value=0.01 a.u.) and scatter plots between the CdSe/ZnS QDs@MPA and FNAC. (h) Fourier transform infrared (FT-IR) spectra and (i) fluorescence lifetime spectra of FNAC, CdSe/ZnS QDs@MPA, and CdSe/ZnS QDs@FNAC.

broadened peak centered at 3364 $cm^{-1}$ confirmed the formation of intermolecular hydrogen bonds (O-H···O) between CdSe/ZnS QDs@MPA and FNAC, which was consistent with the theoretical predictions derived from the IGM. Additionally, compared with FNAC (2.47 ns) and CdSe/ZnS QDs@MPA (3.41 ns), the fluorescence lifetime of CdSe/ZnS QDs@FNAC decreased to 2.00 ns, confirming that non-radiative transitions occurred when CdSe/ZnS QDs@MPA self-assembled with FNAC, thereby triggering the PET process (Figure 2i).

### 3.3 Fluorescence Detection and Discrimination of $KMnO_4$

To investigate the fluorescence response properties of FNAC, CdSe/ZnS QDs@MPA, and CdSe/ZnS QDs@FNAC toward $KMnO_4$ at varying concentrations, a series of $KMnO_4$ solutions with concentrations ranging from 0 to 90.90 μM were prepared. Specifically, upon the addition of 0.90 μM $KMnO_4$, the FNAC system exhibited a distinct cyan fluorescence, whose brightness increased progressively with increasing $KMnO_4$ concentration, whereas the inherent red fluorescence of the CdSe/ZnS QDs@MPA system gradually diminished with increasing $KMnO_4$ concentration (**Figure 3**ai and 3aii). By contrast, as the concentration of $KMnO_4$ increased from 0 to 27.27 μM, the reddish-purple fluorescence gradually faded, with further elevation in concentration, green fluorescence emerged and gradually intensified (Figure 3aiii). To quantify this visual evolution, the RGB values extracted from the fluorescence images of the FNAC, CdSe/ZnS QDs@MPA, and CdSe/ZnS QDs@FNAC were mapped onto a CIE 1931 chromaticity diagram (Figure 3b). The analysis revealed that the chromaticity coordinates of CdSe/ZnS QDs@MPA were distributed in the red region, those of FNAC were concentrated in the blue and green regions, while the self-assembled CdSe/ZnS QDs@FNAC system spanned both the red and green regions. Notably, the geometric distance between the two most separated chromaticity coordinates of the CdSe/ZnS QDs@FNAC system was 3 times that of CdSe/ZnS QDs@MPA and 1.5 times that of FNAC, respectively. This substantial chromatic shift signified superior visual discrimination performance, confirming the advantages of the dual-signal ratiometric strategy.

The corresponding fluorescence spectra demonstrated that upon contact between FNAC and $KMnO_4$, a new fluorescence emission peak attributable to FNOH appeared at 521 nm, and its intensity increased progressively as the concentration of $KMnO_4$ increased (Figure 3c). By contrast, the fluorescence emission intensity of the CdSe/ZnS QDs@MPA at 639 nm decreased gradually with increasing $KMnO_4$ concentration,

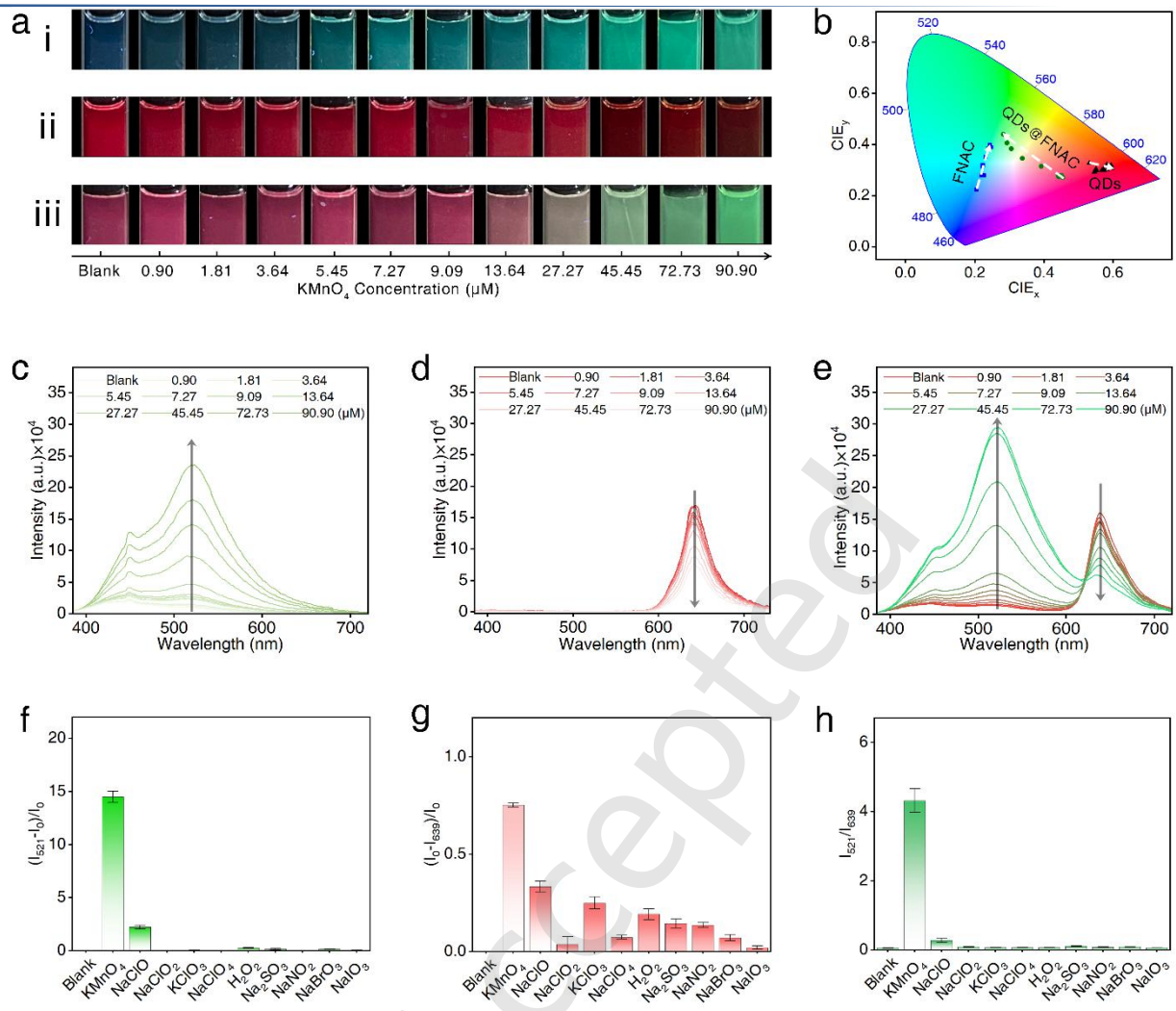


**Figure 3.** (a) Fluorescent images and of (i) FNAC, (ii) CdSe/ZnS QDs@MPA, (iii) CdSe/ZnS QDs@FNAC in response to different concentrations of $KMnO_4$ (0-90.90 μM) under excitation at 365 nm. The corresponding (b) visual perceptual differences evaluation based on the CIE 1931 chromaticity diagram and (c-e) fluorescence spectra. Histogram of the intensity ratio of $(I_{521}-I_0)/I_0$ (f) FNAC, $(I_0-I_{639})/I_0$ (g) CdSe/ZnS and $I_{521}/I_{639}$ (h) CdSe/ZnS QDs@FNAC in response to various oxidants (1 mM) and $KMnO_4$ (1 mM). Note that the excitation wavelength is 365 nm, and the standard deviations were obtained from three repeated measurements.

and the intensity dropped to 50% of its initial value when the $KMnO_4$ concentration reached 90.90 μM (Figure 3d). For the CdSe/ZnS QDs@FNAC system, as the concentration of $KMnO_4$ increased, a new fluorescence emission peak emerged at 521 nm and intensified progressively, whereas the emission peak at 639 nm gradually weakened, which was consistent with the behavior observed when FNAC and CdSe/ZnS QDs@MPA were present individually (Figure 3e).Collectively, these results indicate that $KMnO_4$ effectively disrupts the intermolecular hydrogen bonds between FNAC and CdSe/ZnS QDs@MPA, which then sequentially undergo redox reactions with FNAC and CdSe/ZnS QDs@MPA, respectively, thereby inducing the corresponding variations in the fluorescence signals. For the CdSe/ZnS QDs@FNAC system, $KMnO_4$ triggered a robust dual-signal ratiometric fluorescence response, with an excellent linear correlation established between the emission intensity ratio ($I_{521}/I_{639}$) and $KMnO_4$ concentration over the range of 5.45-90.90 μM (Figure S7). The limit of detection (LOD) was determined to be as low as 4.80 nM, calculated using the formula LOD=3σ/k, in which σ=0.000085 represents the standard deviation of the emission intensity ratio($I_{521}/I_{639}$) of the CdSe/ZnS QDs@FNAC solution derived from 11 replicate measurements, and k=0.0531 denotes the slope of the linear fitting curve. This value is well below the maximum allowable concentration of $KMnO_4$ (0.025 mM) specified in the recommended sanitary standards for drinking water.

To further elucidate the reaction kinetics of CdSe/ZnS QDs@FNAC toward $KMnO_4$, the time-dependent fluorescence evolution was tracked using optical images extracted from the video recording under excitation with a 365 nm UV lamp (Figure S8). After the addition of $KMnO_4$, the red fluorescence gradually weakened, with green fluorescence emerging at 1 s. Over time, the red fluorescence completely faded away, while the green fluorescence continued to increase progressively. Moreover, the proposed dual-signal ratiometric system designed in this work outperformed previously reported fluorescent nanosensors in terms of response time and detection sensitivity. Such performance enhancements were primarily driven by the accelerated redox kinetics of $KMnO_4$ within the acidic microenvironment and the superior SNR afforded by the dual-signal response mode (Table S2). By extracting RGB values from optical images and plotting them with time as the abscissa and the G/R ratio as the ordinate, the variation between the two parameters within 3 s followed a linear function with $R^2$=0.9129,

and then gradually stabilized, indicating that the reaction between CdSe/ZnS QDs@FNAC and $KMnO_4$ can reach equilibrium relatively quickly (Figure S9). Furthermore, the selectivity of the CdSe/ZnS QDs@FNAC toward $KMnO_4$ was evaluated against 23 types of interferents, including oxidants ($H_2O_2$, $NaNO_2$, and NaClO), reductants, and common anions and cations. The fluorescence spectra revealed that only $KMnO_4$ could induce CdSe/ZnS QDs@FNAC to produce an emission peak at 521 nm, while quenching the fluorescence at 639 nm, whereas the effects of other interferents on the optical properties of CdSe/ZnS QDs@FNAC were statistically insignificant (Figure S10). The histogram of the emission intensity ratio ($I_{521}/I_{639}$) for each analyte also exhibits the most prominent response toward $KMnO_4$, thus confirming the excellent selectivity of CdSe/ZnS QDs@FNAC for $KMnO_4$ (Figure 3f–3h). Notably, the response intensity of FNAC toward $KMnO_4$ at 521 nm was approximately five times that toward NaClO, and for CdSe/ZnS QDs@MPA, this value was only approximately two times (Figures S11 and S12). By contrast, for the CdSe/ZnS QDs@FNAC system, the ratiometric intensity ratio ($I_{521}/I_{639}$) in the presence of $KMnO_4$ was nearly 28 times of that observed with NaClO. To further evaluate the influence of potential interferents on the detection of $KMnO_4$ by CdSe/ZnS QDs@FNAC, $KMnO_4$ (1mM) was individually mixed with 23 interferents (10 mM) individually and each mixture was subsequently added to the CdSe/ZnS QDs@FNAC (Figure S13). The characteristic ratiometric fluorescence response was maintained, and the emission intensity ratio ($I_{521}/I_{639}$) remained above 71.85% compared with that of $KMnO_4$ alone, indicating that the CdSe/ZnS QDs@FNAC exhibited excellent anti-interference capability for $KMnO_4$, even in complex sample matrices (Figure S14). Furthermore, the CIE 1931 chromaticity diagram reveals a distinct segregation of data points: all samples containing $KMnO_4$ cluster tightly in the green region, whereas those devoid of the target analyte remain localized in the red region (Figure S15). This clear chromatic separation confirms the superior naked-eye distinguishability of the dual-signal system, validating its feasibility for the high-fidelity identification of $KMnO_4$ with exceptional SNR. In summary, unlike traditional single-fluorophore modulation, the proposed dual-signal response mode triggers simultaneous and divergent "turn-on/turn-off" transitions. By maximizing the differential between the two emission channels, this approach effectively amplifies the dynamic range and ensures robust self-calibration, thereby overcoming the inherent sensitivity constraints of conventional QD-based ratiometric platforms.

### 3.4 Sensing Mechanism Exploration of CdSe/ZnS QDs@FNAC for the Detection of $KMnO_4$

A computational model of spherical $Cd_{33}Se_{33}$ QDs with a diameters of approximately 1.3 nm was constructed, as these QDs have been verified to exist and is referred to as a "magic-sized clusters" (Figure S16). Subsequently, three MPA ligands were anchored onto the surface of the $Cd_{33}Se_{33}$ QDs *via* Cd–S bonds (denoted as $Cd_{33}Se_{33}$ QDs@3MPA), and the geometry of the systemwas optimized to minimize the number of dangling surface bonds (**Figure 4**a). The density of states (DOS) and partial density of states (PDOS) of the $Cd_{33}Se_{33}$ QDs@3MPA model revealed a distinct energy gap between the highest occupied molecular orbital (HOMO) and the lowest unoccupied molecular orbital (LUMO) (Figure 4b, Table S3). According to the Natural Transition Orbital (NTO) analysis of the optimized excited state structure of $Cd_{33}Se_{33}$ QDs@3MPA, the electronic transition from the ground state ($S_0$) to the lowest singlet excited state ($S_1$) is dominated almost exclusively by the HOMO–LUMO transition (99.9955%). This indicates that the lowest-energy excitation process of the $Cd_{33}Se_{33}$ QDs@3MPA system exhibited an exceptionally high degree of orbital specificity (Table S4). This phenomenon mitigates complex non-radiative decay pathways via two primary mechanisms: first, the near-complete absence of orbital mixing eliminates energy losses stemming from multi-orbital coupling; and second, the partial spatial separation of charge carriers effectively suppresses Auger recombination, which would otherwise be a dominant non-radiative channel. These results provide a clear rationale for the sharp emission profile and high photoluminescence quantum efficiency obtained for the CdSe/ZnS QDs@MPA system. Frontier molecular orbital analysis reveals that the HOMO–LUMO electronic transition energy of $Cd_{33}Se_{33}$ QDs@3MPA is 1.93 eV, accompanied by an electron density transfer from the MPA ligand to $Cd_{33}Se_{33}$ QDs. The emission peak was calculated to be 642 nm using the formula $Eg=hc/\lambda$, which is consistent with the experimental results (639 nm) (Figure 4c). The HOMO–LUMO electronic transition energy of FNAC is 4.67 eV, with the accompanying electron density transferring from the naphthyl group to the aldehyde and acrylate groups. Notably, the LUMO of $Cd_{33}Se_{33}$ QDs@3MPA is -3.68 eV, while that of FNAC is -1.94 eV, and this energy level difference drives the electron transfer from the LUMO orbital of excited-state FNAC to that of $Cd_{33}Se_{33}$ QDs@3MPA, thereby triggering the PET process. After reacting with $KMnO_4$, the MPA ligands on the surface of $Cd_{33}Se_{33}$ QDs@3MPA are etched, and the HOMO–LUMO electronic transition energy increases to 3.19 eV, which makes electron–hole pairs more prone to non-radiative recombination, further resulting in fluorescence quenching. The HOMO–LUMO electronic transition energy of the reaction product (FNOH) is 4.60 eV, accompanied by electron density transfer from the hydroxyl group to the aldehyde group. Although the LUMO of FNOH (–1.67 eV) is higher than that of $Cd_{33}Se_{33}$ QDs (–3.46 eV), the surface ligands of the QDs were etched away, preventing hydrogen bonding with FNOH and thus the close proximity required for PET; therefore, fluorescence was not quenched.

Based on the atom-like atomic orbital contribution decomposition of different molecular orbitals for $Cd_{33}Se_{33}$ QDs@3MPA and $Cd_{33}Se_{33}$ QDs, a comprehensive analysis was performed by integrating the orbital contribution curves of different fragments, the color distribution of discrete vertical lines, and the orbital decomposition results (Figure 4d). The HOMO of $Cd_{33}Se_{33}$ QDs@3MPA was predominantly contributed by MPA, whereas its LUMO was mainly derived from the Se 4p and Cd 5p orbitals, resulting in a low degree of spatial overlap between electrons and holes, thereby enabling the effective suppression of nonradiative recombination processes such as Auger recombination. When the electrons transitioned from the excited state to the ground state, they tended to undergo radiative recombination accompanied by

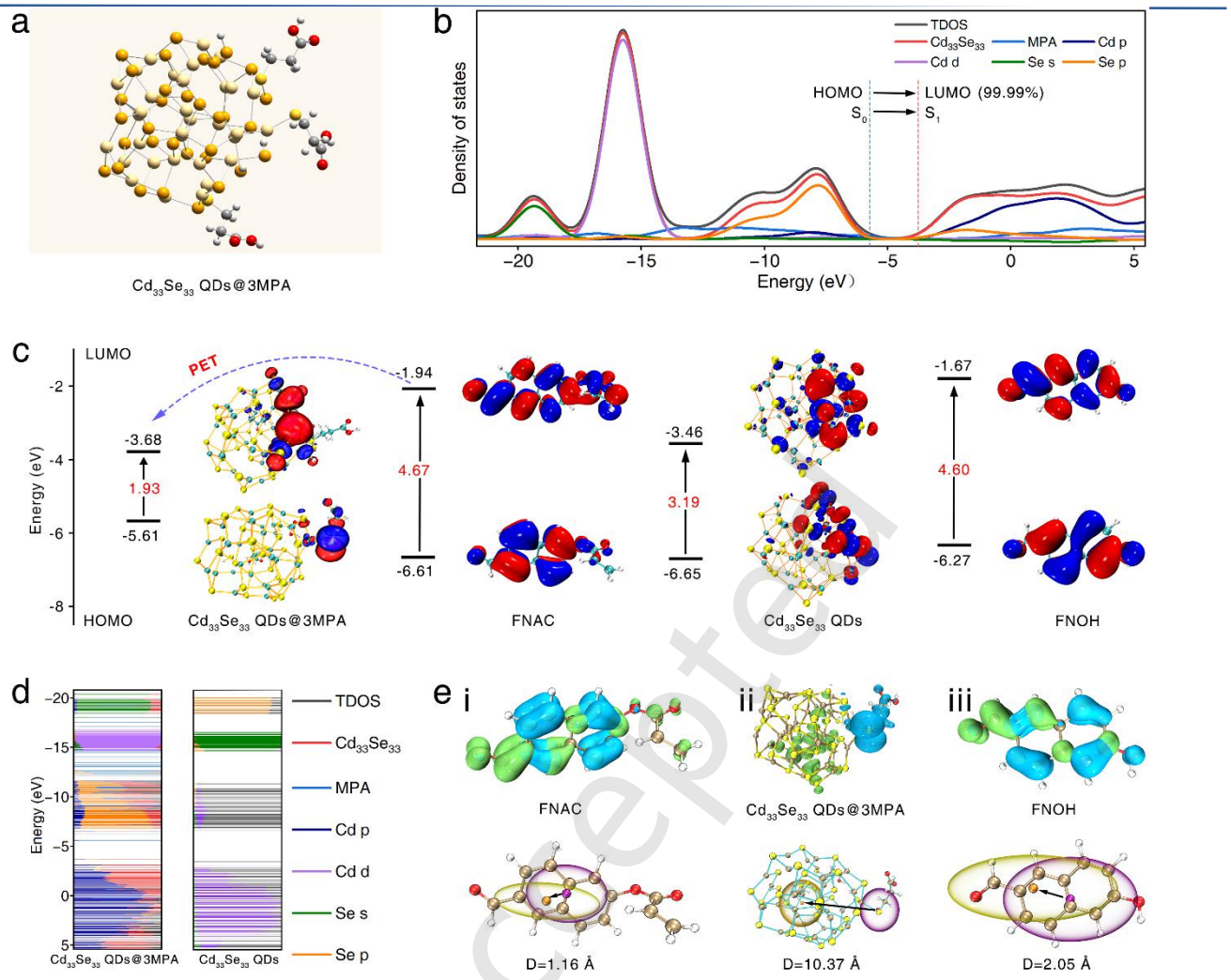


**Figure 4.** (a) The computational model, and (b) density of states (DOS) and partial density of states (PDOS) of the $Cd_{33}Se_{33}$ QDs@3MPA. (c) Electron-density distribution and the corresponding energy diagrams of the main molecular orbitals of $Cd_{33}Se_{33}$ QDs@OA, $Cd_{33}Se_{33}$ QDs@3MPA, FNAC, and FNOH, respectively. Red and blue regions denote the positive and negative orbital phases, respectively. (d) The PDOS of $Cd_{33}Se_{33}$ QDs@3MPA and $Cd_{33}Se_{33}$ QDs. (e) The hole (blue region) and electron (green region) distributions of (i) FNAC, (ii) $Cd_{33}Se_{33}$ QDs@3MPA, (iii) FNOH. The corresponding $C_{hole}$ and $C_{ele}$ diagrams were smoothly generated from the hole and electron distributions, the centroids of $C_{hole}$/$C_{ele}$ were marked by purple and orange spheres, respectively, and the charge transfer distance between them is denoted as D.

photon emission, enhancing the red fluorescence emission properties of $Cd_{33}Se_{33}$QDs@3MPA. By contrast, both the HOMO and LUMO of the $Cd_{33}Se_{33}$ QDs are contributed by the Cd 5p and the Se 4s orbitals, and their high compositional similarity leads to a significant enhancement in the spatial overlap between electrons and holes. Consequently, this facilitates the occurrence of non-radiative recombination processes such as Auger recombination, resulting in a substantial reduction in the probability of radiative recombination and ultimately endowing the QDs with weak fluorescence emission properties. Furthermore, analysis of the electron-hole distribution and the centroids of $C_{hole}$ and $C_{ele}$ reveals that the hole in FNAC is primarily localized on the naphthalene group, while the electrons are distributed over the acryloyl and aldehyde regions (with a centroid distance D = 1.16 Å), exhibiting characteristics of localized excitation (Figure 4ei). For $Cd_{33}Se_{33}$ QDs@3MPA, the holes are mainly distributed in the MPA ligands, while electrons are concentrated within the $Cd_{33}Se_{33}$ QDs core, with a D value of 10.37 Å (Figure 4eii). When the –COOH groups on the surface of $Cd_{33}Se_{33}$ QDs@MPA interacted with the –CHO groups in FNAC via hydrogen bonding to form the self-assembled $Cd_{33}Se_{33}$ QDs@FNAC, the electrons in the –CHO groups were likely to transfer to the MPA ligands under excitation, thereby inducing the PET process. The electrons of the product FNOH are mainly concentrated in segment 2 (red area), while holes are primarily localized in segments 4 and 2 (dark blue area). This indicates that electrons transfer from segment 4 to segment 2, resulting in a D value 0.89 Å higher than that of FNOH (Figure 4eiii, Figure S17). Furthermore, the oxidation of FNAC by $KMnO_4$ induced the cleavage and hydrolysis of its acrylate bonds, suppressing the TICT process and enabling the fluorescence emission of FNOH.

Analysis of the morphological transformation of CdSe/ZnS QDs@FNAC after the reaction with $KMnO_4$ revealed that the interaction process was primarily attributed to three synergistic effects induced by $KMnO_4$: first, $KMnO_4$ disrupts the CdSe/ZnS QDs@FNAC assembly; second, the MPA on the QDs surface is etched away, leading to the dissociation of QDs aggregates; and third, the oxidation of the FNAC leads to the release of hydroxyl groups, which enhances intermolecular hydrogen bonding interactions and thereby preserves the rod-like structure (Figures

S18–S20). Additionally, IGM analysis confirmed that the –COOH groups in MPA formed strong hydrogen bonds with the –CHO groups in FNOH (Figure S21). The scatter plots of these interactions exhibit spikes around the negative sign ($\lambda_2$) ρ (−0.093) and a high δ value (0.117), where the interaction strength is higher than that of the CdSe/ZnS QDs@FNAC self-assembled system, thereby driving the change in morphology. After adding $KMnO_4$ to the CdSe/ZnS QDs@FNAC, the fluorescence lifetime of the system increased from 2.00 ns (before the reaction with $KMnO_4$) to 3.84 ns, which verifies the suppression of the PET process (Figure S22).

### 3.5 CdSe/ZnS QDs@FNAC Hydrogel-Based Ratiometric Fluorescence Sensing Chip for Identification of $KMnO_4$ Particle

To further investigate the practical applicability of CdSe/ZnS QDs@FNAC, a self-developed portable detector integrated with a sensing chip, camera, and UV lamp was employed for the detection of $KMnO_4$ in unknown particulate samples (**Figure 5**a). The sensing chip was fabricated by individually encapsulating CdSe/ZnS QDs@FNAC, FNAC, CdSe/ZnS QDs@MPA, the previously reported probe PA, and DMA-CN into a hydrogel-based supporting matrix via the solvent exchange method, followed by subsequent integration into the sensing array using hot melt sealing technology (Figures S23–S25). Real-time monitoring images extracted from dynamic videos of ng-level $KMnO_4$ particles of varying sizes showed that regardless of $KMnO_4$ particle dimensions, the CdSe/ZnS QDs@FNAC-embedded hydrogel sensor immediately quenched red fluorescence and emitted green fluorescence upon contact with $KMnO_4$ particles (Figure 5b). Notably, the mass of individual $KMnO_4$ particles was estimated from the initial purple spots, which were approximated as spherical, and the corresponding time was defined as 0 s. Concurrently, the fluorescent area expanded progressively over time owing to the dissolution and subsequent diffusion of $KMnO_4$, and the size of $KMnO_4$

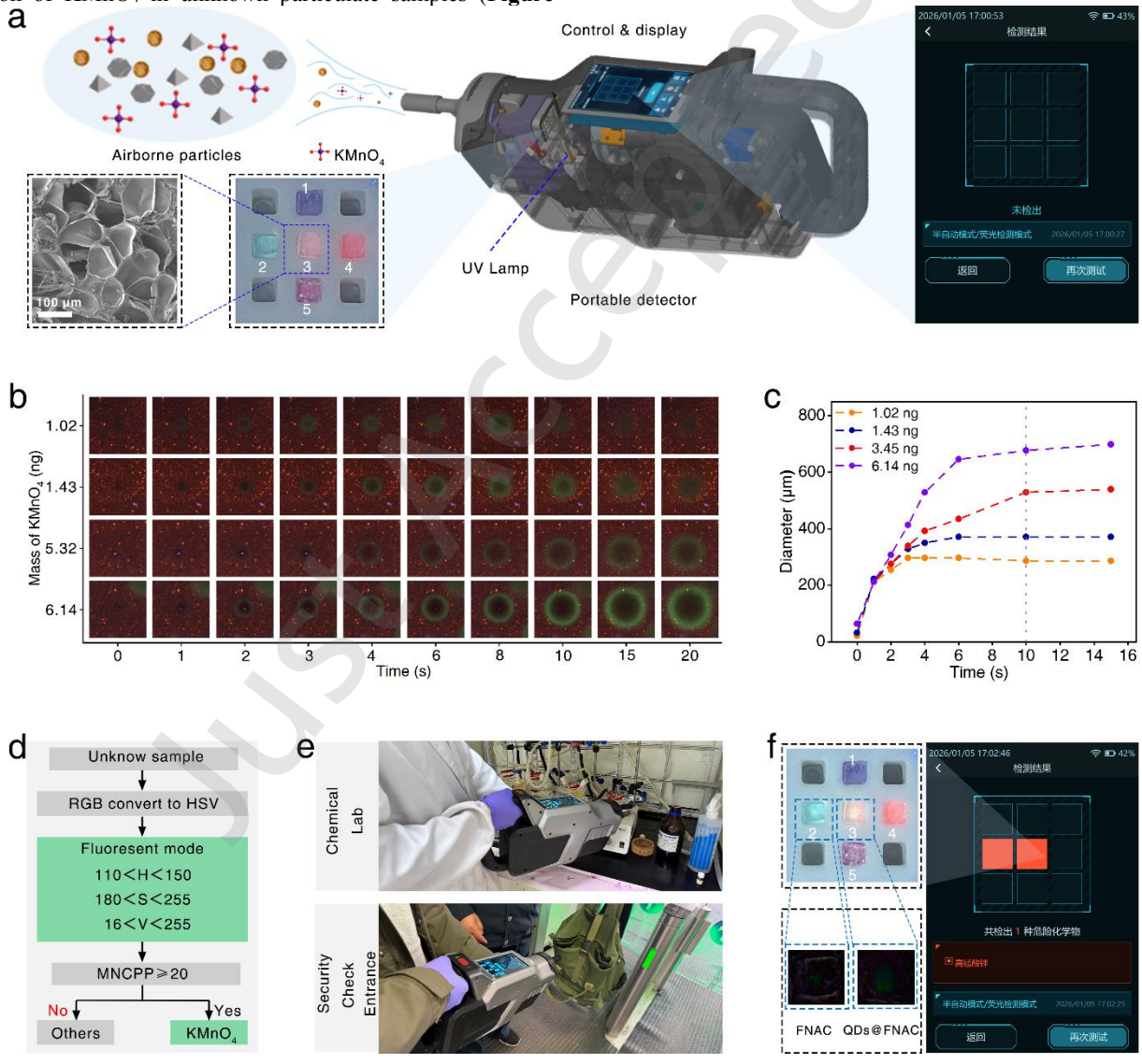


**Figure 5.** (a) Schematic illustration of the portable detector for on-site determination of $KMnO_4$ particles (Region 1 to previously reported probe PA, Region 2 to FNAC, Region 3 to CdSe/ZnS QDs@FNAC, Region 4 to CdSe/ZnS QDs@MPA, and Region 5 to previously reported probe DMA-CN). (b) Time-lapse images extracted from the video of the sensing process captured under an industrial camera. (c) The corresponding diffusion diameters as a function of time. (d) Logical discriminant flowchart. (e) $KMnO_4$ detection in simulated scenarios. (f) The resulting $KMnO_4$-positive readout on the display screen, the sensor array image obtained after $KMnO_4$ collection under 365 nm UV illumination and the color difference maps of FNAC and CdSe/ZnS QDs@FNAC before and after detection of $KMnO_4$.

particles correlated with both the size of the characteristic fluorescence area and intensity. The correlation between the diffusion diameters at 15 s and the mass of $KMnO_4$ particles revealed that as the mass of $KMnO_4$ particle increases, the growth rate of the ultimate diffusion diameter gradually decreases, whereas all particles essentially reach a diffusion equilibrium state within 6 s (Figure 5c). In addition, a distinct linear correlation was observed between the particle mass and diffusion diameter, further validating the reliability of the proposed method for the detection of $KMnO_4$ particles (Figure S26).

This hydrogel-based sensing chip exhibited a distinct ratiometric fluorescence response exclusively upon contact with $KMnO_4$, whereas the fluorescence changes induced by the other 19 interferents were negligible (Figure S27). Furthermore, the G/R values extracted from the optical images revealed that the G/R value for $KMnO_4$ detection was at least 2-fold higher than those for other interferents, further demonstrating the excellent selectivity and reliability of the hydrogel-based sensor (Figure S28). The hydrogel-based sensing array was inserted into the portable detector, after the unknown particles were adsorbed onto the hydrogel-based sensing chip via suction sampling, the particles came into contact with the CdSe/ZnS QDs@FNAC, resulting in the corresponding characteristic fluorescence emission changes. The color change of the sensing array was recorded by the detector integrated optical system, and the acquired images were subsequently analyzed through a data processing module using color (HSV) thresholds and the minimum number of connected pixel points (MNCPP) that interacted with the characteristic signals (Figure 5d). This process enables the accurate identification of target analytes, with the subsequent transmission of the results to both the display unit and cloud storage platform. In the simulated scenario, after the $KMnO_4$ particles were adsorbed onto the sensing array, the portable detector generated a positive alarm signal on the screen within 7 s (Figure 5e). Moreover, the images captured by the built-in camera revealed that the hydrogel loaded with CdSe/ZnS QDs@FNAC and FNAC immediately exhibited green fluorescence at the edge of the $KMnO_4$ containing region respectively, which was consistent with the response of the CdSe/ZnS QDs@FNAC-embedded hydrogel sensing chip and that of FNAC alone (Figure 5f). Notably, to reduce the background interference, a color difference map was generated by subtracting the initial fluorescence optical image from the images obtained after detection of $KMnO_4$. The color-difference map of CdSe/ZnS QDs@FNAC exhibited more distinct variations than that of FNAC alone, demonstrating the superior visual detection performance of the self-assembled CdSe/ZnS QDs@FNAC system for $KMnO_4$. The portable detector also displayed positive signals in the corresponding regions, demonstrating that the CdSe/ZnS QDs@FNAC dual-signal response system designed in this study has distinct advantages over the CdSe/ZnS QDs@MPA quenching system, the FNAC fluorescence-on probe, and other previously reported ratiometric fluorescence systems[30, 31]. Thus, the present strategy, featuring a dual-signal response mode with a high SNR, not only facilitates on-site visual monitoring of $KMnO_4$ particles but also provides a novel approach for the development of highly sensitive, field-deployable detection platforms for environmental or industrial applications.

## 4 Conclusions

we successfully demonstrated a “microenvironment-assisted synergistic assembly” strategy for constructing a robust dual-signal ratiometric sensing platform (CdSe/ZnS QDs@FNAC). Unlike conventional systems in which nanocarriers serve merely as inert scaffolds, the carboxyl-terminated CdSe/ZnS QDs@MPA in our design plays a pivotal triple role: serving as a hydrogen-bonded anchors for FNAC, conferring water solubility, and enhancing the oxidative potency of $KMnO_4$. Upon reacting with $KMnO_4$, the hydrogen-bonded assembly dissociates, disrupting the initial PET process, which triggers the oxidative etching-induced quenching of the QDs while concurrently suppressing the TICT state of the released FNAC probe to activate its green fluorescence. This ratiometric fluorescence system with a dual-signal response mode has been demonstrated to exhibited excellent sensing performance for $KMnO_4$, including a fast response speed (1 s), high sensitivity (4.80 nM), high SNR ratio, and negligible interference from other oxidants. The feasibility of this dual-signal strategy for monitoring trace $KMnO_4$ particles was validated by integrating the probe into a portable device and testing it under practical scenarios. We expect that the present CdSe/ZnS QDs@FNAC design strategy will provide inspiration for the customization of a ratiometric fluorescence sensing system with high SNR ratio and specific sensing capabilities.

**Electronic Supplementary Material:** Supplementary material ($^1$H NMR, $^{13}$C NMR, HRMS, SEM, TEM, XPS, Fluorescence emission spectrum, Fragment transition density matrix maps[54,55], fluorescence lifetime spectrum, CIE 1931 chromaticity diagram, scatter graphs) is available in the online version of this article at https://doi.org/10.26599/NR.2026.94908873.

## Data availability

All data needed to support the conclusions in the paper are presented in the manuscript and/or the Electronic Supplementary Material. Additional data related to this paper may be requested from the corresponding author upon request.

## Acknowledgements

This work was supported by the National Natural Science Foundation of China (52172168, 22174159), Key Research Project of Chinese Academy of Sciences (KGFZD-145-25-21-01), Natural Science Foundation of Xinjiang (2025D01E54), Central Government Guidance Fund for Local Sci-Tech Development (ZYYD2025JD06), Tianshan Talents Plan (2022TSYCCX0074), Tianshan Innovation Team Plan (2022TSYCTD0020), Youth Innovation Promotion Association of the Chinese Academy of Sciences (2022441).

## Declaration of competing interest

All the contributing authors report no conflict of interests in this work.

## Author contribution statement

Rongchao Zhu: Writing-original draft, software, methodology, investigation, data curation, formal analysis, conceptualization. Zhenzhen Cai: Writing-review & editing, writing-original draft, supervision, methodology, investigation, funding acquisition, conceptualization. Xu Cheng: Data curation, formal analysis. Luyan Yang: Formal analysis, funding acquisition. Baiyi Zu:

Formal analysis, funding acquisition. Xincun Dou: Writing-review & editing, supervision, methodology, investigation, funding acquisition, conceptualization. All the authors have approved the final manuscript.

## Informed consent
Not applicable

## Ethics statement
Not applicable

## Use of AI statement
None

## References

[1] Yuan, S.; Ma, C.; Fetaya, E.; Mueller, T.; Naveh, D.; Zhang, F.; Xia, F. Geometric Deep Optical Sensing. *Science* **2023**, 379, 1103–1112.

[2] Yang, Z.; Xu, T.; Zhang, S.; Li, H.; Ji, Y.; Jia, X.; Li, J. Multifunctional N,S-Doped and Methionine Functionalized Carbon Dots for On-Off-On $Fe^{3+}$ and Ascorbic Acid Sensing, Cell Imaging, and Fluorescent Ink Applying. *Nano Res.* **2022**, 16, 5401–5411.

[3] Yang, Z.; Qian, J.; Zhao, S.; Lv, Y.; Feng, Z.; Wang, S.; He, H.; Zhang, S.; Liu, H.; Yang, B. Highly Sensitive Thianthrene Covalent Trimer Room-Temperature Phosphorescent Materials for Low-Concentration Oxygen Detection. *Angew. Chem. Int. Ed.* **2025**, 64, e202424669

[4] Wang, Y.; Yao, J.; Wu, S.; Zhi, C.; Yin, L.; Song, Z.; Wang, J.; Ling, L.; Ma, Y.; Zhang, D.; Li, J.; Li, L.; Chen, B. Encapsulation of Metal Nanoclusters into Hydrogen-Bonded Organic Frameworks for Double-Response-Reverse Ammonia Fluorescence Sensing. *Chem* **2025**, 11, 102457–102467.

[5] Ren, J.; Li, Z.; Qu, B.; Meng, L.; Bai, L.; Sun, J.; Zhang, Z.; Qu, Y.; Jing, L. Visual Eosin Y‐Based Photosensitization Sensing Systems for Ultrasensitive Detection of Diclofenac with Dingle‐Atom Co-$N_2O_2$ Site-Immobilized G-$C_3N_4$ Nanosheets. *Adv. Mater.* **2024**, 36, 2404392

[6] Zhu, X.; Li, H.; Wu, T.; Zhao, H.; Wu, K.; Xu, W.; Qin, F.; Chen, W.; Zheng, J.; Liu, Q. In Situ Decorating the Surface and Interlayer of Montmorillonite with $Co_{0.5}Ni_{0.5}Fe_2O_4$ Nanoparticles: A Sustainable, Biocompatible Colorimetric Platform for $H_2O_2$ and Acetylcholine. *Nano Res.* **2022**, 15, 9319–9326.

[7] Chu, J.; Ejaz, A.; Lin, K. M.; Joseph, M. R.; Coraor, A. E.; Drummond, D. A.; Squires, A. H. Single-Molecule Fluorescence Multiplexing by Multi-Parameter Spectroscopic Detection of Nanostructured FRET Labels. *Nat. Nanotechnol.* **2024**, 19, 1150–1160.

[8] Zhao, X.; Liu, X.; Chen, D.; Shi, G.; Li, G.; Tang, X.; Zhu, X.; Li, M.; Yao, L.; Wei, Y.; Song, W.; Sun, Z.; Fan, X.; Zhou, Z.; Qiu, T.; Hao, Q. Plasmonic Trimers Designed as Sers-Active Chemical Traps for Subtyping of Lung Tumors. *Nat. Commun.* **2024**, 15, 5855–5865.

[9] Zhou, H.; Qi, G.; Li, W.; Wang, Y.; Yuan, Z. Electrolyte-Gated Srcoox Fet Sensor for Highly Sensitive Detecting pH in Extreme Alkalinity Solution. *Nano Res.* **2023**, 17, 3079–3086.

[10] Hong, X.; Liu, G.; Yang, C.; He, J.; Wu, H.; Chen, H.; Kandegama, W.; Gao, Y.; Li, J.; Hao, G. Macrocyclic Fluorescent Probes for the Detection of Environmental Pollutants: A Comprehensive Review. *Coord. Chem. Rev.* **2025**, 542, 216896–216935.

[11] Liu, K.; Zhang, J.; Shi, Q.; Ding, L.; Liu, T.; Fang, Y. Precise Manipulation of Excited-State Intramolecular Proton Transfer Via Incorporating Charge Transfer toward High-Performance Film-Based Fluorescence Sensing. *J. Am. Chem. Soc.* **2023**, 145, 7408–7415.

[12] Zhang, T.; Yin, Y.; Yang, X.; Li, N.; Wang, W.; Yang, Y.; Tian, W.; Bai, F.; Zou, B. Space-Confined Charge Transfer Turns on Multicolor Emission in Metal-Organic Frameworks Via Pressure Treatment. *Nat. Commun.* **2025**, 16, 4166–4175.

[13] Miao, X.; Wu, C.; Xia, Y.; Yu, S.; Li, F.; Zhang, M. Ratiometric Fluorescence Probes for Visible Detection and Accurate Identification of Mpea Vapor. *Nat. Commun.* **2024**, 15, 10641–10653.

[14] Tao, F.; Yisimayili, N.; Zhao, C.; Gu, C.; Du, Y.; Hu, Y.; Dou, X.; Zu, B. Steric-Engineered Thermodynamic Gating: Metastable Assemblies for Chemical-Class Discrimination of Synthetic Cannabinoids. *Angew. Chem. Int. Ed.* **2026**, 65, e3463809.

[15] Zhang, Y.; Cheng, X.; Zhao, C.; Song, C.; Li, J.; Zhu, R.; Ning, J.; Dou, X.; Cai, Z. Stepwise Conformational Restriction of Acylhydrazone-Based Molecules for High Signal-to-Noise Fluorescent Recognition of Synthetic Cannabinoid Fub-Inaca. *Angew. Chem. Int. Ed.* **2026**, 65, e3262519.

[16] Martin Jimenez, A.; Baltes, M.; Cornelius, J.; Aközbek, N.; Coppens, Z. J. Single-Shot Phase Diversity Wavefront Sensing in Deep Turbulence Via Metasurface Optics. *Nat. Photonics* **2025**, 19, 1315–1322.

[17] Srinivasan, P.; P Sivaraman, S.; Mohan, A. M.; Madhu, D. K.; K Chinaraga, P.; Rao, C. V. S. B.; Nagarajan, S.; Deivasigamani, P. Chromoionophoric Molecular Probe Infused Bimodal Porous Polymer Rostrum as Solid-State Ocular for the Selective and Expeditious Optical Sensing of Ultra-Trace Toxic Mercury Ions. *J. Hazard. Mater.* **2024**, 478, 135483–135496.

[18] Zhao, P.; Lu, H.; Chen, C. Recent Advances in Preparation and Applications of White Circularly Polarized Luminescent Materials. *Chem. Soc. Rev.* **2025**, 54, 8534–8555.

[19] Zheng, W.; Li, T.; Jin, F.; Qian, L.; Ma, J.; Wei, Z.; Ma, X.; Wang, F.; Sun, J.; Yuan, T.; Wang, T.; Feng, Z. Q. Interfacial Polarization Locked Flexible B‐Phase Glycine/$Nb_2CT_x$ Piezoelectric Nanofibers. *Small* **2024**, 20, 2308715–2308725.

[20] Park, S.; Kwon, N.; Lee, J.; Yoon, J.; Shin, I. Synthetic Ratiometric Fluorescent Probes for Detection of Ions. *Chem. Soc. Rev.* **2020**, 49, 143–179.

[21] Qi, Y.; Li, Y.; Tan, M.; Yuan, F.; Murthy, N.; Duan, Y.; Zhu, H.; Yang, S. Recent Advances in Organic Near-Infrared Ratiometric Small-Molecule Fluorescent Probes. *Coord. Chem. Rev.* **2023**, 486, 215130–215166.

[22] Fu, Q.; Yang, X.; Wang, M.; Zhu, K.; Wang, Y.; Song, J. Activatable Probes for Ratiometric Imaging of Endogenous Biomarkersin Vivo. *ACS Nano* **2024**, 18, 3916–3968.

[23] Zhao, X.; Wang, Y.; Wen, J.; Cao, L.; Wang, F.; Lei, K.; Fang, R.; Zhou, L.; Li, Y. High-Curvature Interfaces Induce Nondegenerate Splitting of D-Orbital Energy Levels for Enhanced Catalytic Activity. *J. Am. Chem. Soc.* **2025**, 147, 19166–19177.

[24] Liu, Y.; Teng, L.; Lyu, Y.; Song, G.; Zhang, X.-B.; Tan, W. Ratiometric Afterglow Luminescent Nanoplatform Enables Reliable Quantification and Molecular Imaging. *Nat. Commun.* **2022**, 13, 2216–2228.

[25] Du, Z.; Wang, W.; Luo, S.; Zhang, L.; Yuan, S.; Hei, Y.; Bao, Z.; Chen, C.; Lin, Y.; Chu, L. Self-Renewable Tag for Photostable Fluorescence Imaging of Proteins. *J. Am. Chem. Soc.* **2023**, 145, 18968–18976.

[26] Cong, H.; Wang, K.; Zhou, Z.; Yang, J.; Piao, Y.; Yu, B.; Shen, Y.; Zhou, Z. Tuning the Brightness and Photostability of Organic Dots for Multivalent Targeted Cancer Imaging and Surgery. *ACS Nano* **2020**, 14, 5887–5900.

[27] Chen, L.; Liu, D.; Peng, J.; Du, Q.; He, H. Ratiometric Fluorescence Sensing of Metal-Organic Frameworks: Tactics and Perspectives. *Coord. Chem. Rev.* **2020**, 404, 213113–213140.

[28] Liu, Y.; Xue, R.; Yan, B. Development and Prospects of Covalent Organic Framework-Based Ratiometric Fluorescent Sensors. *Coord. Chem. Rev.* **2025**, 523, 216280–216294.

[29] Paydar, S.; Feizi, F.; Shamsipur, M.; Barati, A.; Chehri, N.; Taherpour, A.; Jamshidi, M. An Ideal Ratiometric Fluorescent Probe Provided by the Surface Modification of Carbon Dots for the Determination of $Pb^{2+}$. *Sens. Actuators, B: Chem.* **2022**, 369, 132243–132251.

[30] Rehemaitijiang, M.; Li, G.; Zhu, R.; Zu, B.; Dou, X.; Su, Z.; Cai, Z. Triple-Standard Hypochlorite Quantitative Array

Enabled by Precise Stokes Shift Modulation in D-π-A Chemodosimeters. *Anal. Chem.* **2025**, 97, 9462–9470.
[31] Yang, X.; Cai, Z.; Li, D.; Lei, D.; Li, Y.; Wang, G.; Zhang, J.; Dou, X. D-π-A Dual-Mode Probe Design for the Detection of nM-Level Typical Oxidants. *Anal. Chem.* **2022**, 94, 9184–9192.
[32] García de Arquer, F. P.; Talapin, D. V.; Klimov, V. I.; Arakawa, Y.; Bayer, M.; Sargent, E. H. Semiconductor Quantum Dots: Technological Progress and Future Challenges. *Science* **2021**, 373, 640–655.
[33] Mastrippolito, D.; Cavallo, M.; Bahmani Jalali, H.; Eren, G. O.; Bossavit, E.; Zhang, H.; Gemo, T.; Colle, A.; Khalili, A.; Gureghian, C.; Prado, Y.; Silly, M. G.; Pierucci, D.; Di Stasio, F.; Lhuillier, E. Tuning Electronic Properties of II–VI and III–V Narrow Band Gap Nanocrystals through Exposure to Alkali. *Chem. Mater.* **2024**, 36, 11669–11675.
[34] Saadh, M. J.; Ballal, S.; Talib, Z. M.; Karim, S. A.; Qassem, L. Y.; Alasady, A.; Formanova, S.; Sattar, R.; Mahdy, A.; Mizher, R. M.; Idan, A. H.; Muzammil, K.; Alhadrawi, M. Quantum Dot-Based Sensing of Mercury Pollutants: A Comprehensive Review of Inorganic and Carbon-Based Quantum Dots. *Inorg. Chem. Commun.* **2024**, 170, 113232–113244.
[35] Sun, Z.; Xing, H. H.; Qing, M.; Shi, Y.; Ling, Y.; Li, N. B.; Luo, H. Q. From the Perspective of High-Throughput Recognition: Sulfur Quantum Dots-Based Multi-Channel Sensing Platform for Metal Ions Detection. *Chem. Eng. J.* **2023**, 452, 139594–139602.
[36] Naithani, S.; Heena; Sharma, P.; Layek, S.; Thetiot, F.; Goswami, T.; Kumar, S. Nanoparticles and Quantum Dots as Emerging Optical Sensing Platforms for Ni(II) Detection: Recent Approaches and Perspectives. *Coord. Chem. Rev.* **2025**, 524, 216331–216363.
[37] Sun, X.; Xiang, T.; Xie, L.; Ren, Q.; Chang, J.; Jiang, W.; Jin, Z.; Yang, X.; Ren, W.; Yu, Y. Recent Advances in Fluorescent Nanomaterials Designed for Biomarker Detection and Imaging. *Mater. Today Bio* **2025**, 32, 101763–101777.
[38] Cai, X.; Wang, B.; Nian, L.; Cheng, T.; Zhang, C.; Li, L.; Zhang, G.; Xiao, J. Simultaneous Fingerprinting of Multiplex Collagen Biomarkers in Connective Tissues by Multicolor Quantum Dots-Based Peptide Probes. *Mater. Today Bio* **2024**, 26, 101026–101035.
[39] Narasimhappa, P.; Singh, S.; Ramamurthy, P. C. Synthesis of Water-Soluble Cds Quantum Dots for the Fluorescence Detection of Tetracycline. *Environ. Pollut.* **2023**, 338, 122682–122691.
[40] Singh, P. D. D.; Murthy, Z. V. P.; Kailasa, S. K. Zinc Nitride Quantum Dots as an Efficient Probe for Simultaneous Fluorescence Detection of $Cu^{2+}$ and $Mn^{2+}$ Ions in Water Samples. *Microchim. Acta* **2024**, 191, 161–175.
[41] Ren, W.; Li, J.; Zu, B.; Lei, D.; Dou, X. Design of Highly Efficient Electronic Energy Transfer in Functionalized Quantum Dots Driven Specifically by Ethylenediamine. *JACS Au* **2024**, 4, 545–556.
[42] Mondal, T. K.; Kapuria, A.; Miah, M.; Saha, S. K. Solubility Tuning of Alkyl Amine Functionalized Carbon Quantum Dots for Selective Detection of Nitroexplosive. *Carbon* **2023**, 209, 117972–117984.
[43] Qin, L.; Cao, J.; Lin, D.; Xu, S.; Li, Y.; Jiang, C. A Strecker-Like Reaction Triggering Fluorescent Sensing Platform for Enzyme-Free and Visual Quantitative Monitoring of Carbamates. *Chem. Eng. J.* **2023**, 464, 142550–142557.
[44] Loskutova, A.; Seitkali, A.; Aliyev, D.; Bukasov, R. Quantum Dot-Based Luminescent Sensors: Review from Analytical Perspective. *Int. J. Mol. Sci.* **2025**, 26, 6674–6719.
[45] Huang, H.; Dai, S.; Xie, L.; Deng, W.; Tan, Y.; Xie, Q. Cds Quantum-Dots-Modified $CuBi_2O_4$ Nanorods as Highly Active and Etchable Photocathodic Materials for Sensitive Photoelectrochemical Immunoassay. *Sens. Actuators, B* **2023**, 376, 132981–132987.
[46] Xu, J.; Ji, W.; Zhu, K.; Liu, M.; Gao, H.; Yan, M.; Zeng, Q. Application of Fluorescence Resonance Energy Transfer in Homogeneous Immunoassay Using Quantum Dots. *Coord. Chem. Rev.* **2025**, 542, 216872–216897.
[47] R., A.; Clapp, I. L.; Medintz, B. R.; Fisher, G. P.; Anderson. Can Luminescent Quantum Dots Be Efficient Energy Acceptors with Organic Dye Donors? *J. Am. Chem. Soc.* **2005**, 127, 1242–1250.
[48] Duan, Y.; Tan, J.; Huang, Z.; Deng, Q.; Liu, S.; Wang, G.; Li, L.; Zhou, L. Facile Synthesis of Carboxymethyl Cellulose Sulfur Quantum Dots for Live Cell Imaging and Sensitive Detection of Cr(VI) and Ascorbic Acid. *Carbohydr. Polym.* **2020**, 249, 116882–116890.
[49] Zhang, L.; Wang, Y.; Jia, L.; Bi, N.; Bie, H.; Chen, X.; Zhang, C.; Xu, J. Ultrasensitive and Visual Detection of Tetracycline Based on Dual-Recognition Units Constructed Multicolor Fluorescent Nano-Probe. *J. Hazard. Mater.* **2021**, 409, 124935–124945.
[50] Altintas, Y.; Genc, S.; Talpur, M. Y.; Mutlugun, E. CdSe/ZnS Quantum Dot Films for High Performance Flexible Lighting and Display Applications. *Nanotechnology* **2016**, 27, 295604–295613.
[51] Zhiwei, M.; Liping, T.; Bingbing, L. Highly Efficient Full Color Light-Emitting Diodes Based on Quantum Dots Surface Passivation Engineering. *Org. Electron.* **2019**, 70, 140–148.
[52] Freeman, R.; Finder, T.; Bahshi, L.; Gill, R.; Willner, I. Functionalized CdSe/ZnS QDs for the Detection of Nitroaromatic or Rdx Explosives. *Adv. Mater.* **2012**, 24, 6416–6421.
[53] Wang, Y.; Zheng, K.; Guo, H.; Tian, L.; He, Y.; Wang, X.; Zhu, T.; Sun, P.; Liu, Y. Potassium Permanganate-Based Advanced Oxidation Processes for Wastewater Decontamination and Sludge Treatment: A Review. *Chem. Eng. J.* **2023**, 452, 139529–139545.
[54] Lu, T.; Chen, F. Multiwfn: A Multifunctional Wavefunction Analyzer. *J. Comput. Chem.* **2011**, 33, 580–592.
[55] Humphrey, W. D., A.; Schulten, K. Schulten, K. Vmd: Visual Molecular Dynamics. *J. Mol. Graphics Modell* **1996**, 14, 33.

# Electronic Supplementary Material

# Exact charge transfer control in quantum dots/molecule system–induced large emission contrast for ultrasensitive and anti-interfering detection

Rongchao Zhu[1,2], Zhenzhen Cai[1,✉], Xu Cheng[1,2], Luyan Yang[1], Baiyi Zu[1], and Xincun Dou[1,2,✉]

[1] *Xinjiang Key Laboratory of Trace Chemical Substances Sensing, Xinjiang Technical Institute of Physics and Chemistry, Chinese Academy of Sciences, Urumqi 830011, China*
[2] *Center of Materials Science and Optoelectronics Engineering, University of Chinese Academy of Sciences, Beijing 100049, China*

✉ Address correspondence to Zhenzhen Cai, caizz@ms.xjb.ac.cn; Xincun Dou, xcdou@ms.xjb.ac.cn

Supporting information to https://doi.org/10.26599/NR.2026.94908873



## 1. Experimental Section

### 1.1 Materials and characterization

Unless otherwise noted, all reagents and materials were purchased from commercial sources and used without further purification. Trioctylphosphine (TOP, 90%) was purchased from Sigma-Aldrich (Shanghai) Trading Co., Ltd. Cadmium oxide (CdO, 99.99%), zinc acetate (ZnAc, 99.99%), selenium (Se, 99.99%), 1-dodecanethiol (DDT, 98%), oleic acid (OA, AR grade), and 1-octadecene (1-ODE, 90%) were obtained from Adamas-beta Reagent Co., Ltd. (Shanghai, China). 3-Mercaptopropionic acid (98%) was purchased from Heowns Biochem LLC (Tianjin, China). Tetramethylammonium hydroxide (25 wt% in methanol) was purchased from Thermo Fisher Scientific Co., Ltd. (Shanghai, China). 6-Hydroxy-2-naphthaldehyde, acryloyl chloride, triethylamine, magnesium sulfate ($MgSO_4$), sodium hydroxide (NaOH, 97%), sodium carbonate ($Na_2CO_3$, 99.5%), and sodium bicarbonate ($NaHCO_3$, 99.8%) were purchased from Aladdin Biochemical Technology Co., Ltd. (Shanghai, China). And all organic solvents, including petroleum ether (PE), ethyl acetate (EA), dichloromethane (DCM), acetonitrile (ACN), n-hexane, methanol (MeOH), and ethanol (EtOH) were purchased from Sinopharm Chemical Reagent Co., Ltd.

Using tetramethylsilane (TMS) as an internal standard, $^{1}H$ and $^{13}C$ NMR spectra of probe FNAC were obtained using a Bruker Avance NEO 400 MHz NMR instrument. The high-resolution mass spectra (HRMS) were obtained using a Thermo Scientific Q Exactive Orbitrap. The fluorescence spectra were collected using an Edinburgh FLS1000 fluorescence Spectrophotometer (Edinburgh Instruments, UK), while the ultraviolet-visible (UV-vis) absorption spectra were recorded on a Hitachi U3900 UV-vis spectrophotometer (Hitachi, Japan). The transmission electron microscope (TEM, JEM-F2100F, Japan) and field-emission scanning electron microscope (FE-SEM, JEOL JSM-7610F Plus, Japan) equipped with an energy-dispersive spectrometer (Thermo Scientic ESCALAB Xi, USA) were employed to characterize the morphology and elemental composition of the CdSe/ZnS QDs@OA, CdSe/ZnS QDs@MPA, CdSe/ZnS QDs@FNAC, probe FNAC. The elemental composition and content of CdSe/ZnS QDs@OA, CdSe/ZnS QDs@MPA, CdSe/ZnS QDs@FNAC were determined by X-ray photoelectron spectroscopy (XPS) on a Thermo Scientific Escalab 250 Xi spectrometer, which is equipped with an Al Ka (1486.6 eV) X-ray source (Thermo Scientific, USA). Thermogravimetric analysis (TGA) measurements were performed under a nitrogen atmosphere, with a temperature range up to 1000 °C and a heating rate of 10°C $min^{-1}$, using a Simultaneous Thermal Analyzer (STA 8000, USA). Fourier-transform infrared (FT-IR) spectra were acquired using a PerkinElmer Frontier FTIR spectrometer equipped with a Smart Orbit diamond crystal attenuated total reflectance (ATR) attachment (Waltham, MA, USA). The dynamic color change on the CdSe/ZnS QDs@FNAC paper-based sensor and CdSe/ZnS QDs@FNAC-embedded hydrogel sensor were monitored by a camera (Imavision, MER-2000-5GM/C-P, China) with a minimum resolution of 1.2 μm×1.2 μm. The fluorescent images were captured using an iPhone 14 smartphone (Apple, United States).

### 1.2 Preparation and testing of solutions

**Preparation of the FNAC solution (22.70 μg/mL).** 45.4 mg of FNAC was dissolved in 200 mL of $CH_3CN$ to get the probe FNAC solution (1 mM), 10 mL of the FNAC solution (1 mM) were mixed in 100 mL of an $CH_3CN/H_2O$ mixed solvent with a volume ratio of 3:7 to get the CdSe/ZnS QDs@FNAC solution (22.70 μg/mL).

**Preparation of the CdSe/ZnS QDs@MPA solution (16.00 μg/mL).** 80 mg of CdSe/ZnS QDs@MPA was dissolved in 100 mL of deionized water to get the CdSe/ZnS QDs@MPA solution (0.8 mg/mL), 2 mL of CdSe/ZnS QDs@MPA solution (0.80 mg/mL) were

mixed in 100 mL of an $CH_3CN/H_2O$ mixed solvent with a volume ratio of 3:7 to get the CdSe/ZnS QDs@MPA solution (16.00 μg/mL).

**Preparation of the CdSe/ZnS QDs@FNAC solution (38.70 μg/mL).** 10 mL of the FNAC solution (1 mM) and 2 mL of CdSe/ZnS QDs@MPA solution (0.80 mg/mL) were mixed in 100 mL of an $CH_3CN/H_2O$ mixed solvent with a volume ratio of 3:7 to get the CdSe/ZnS QDs@FNAC solution.

**Fluorescence Spectral testing of the FNAC.** 2.0 mL of the FNAC solutions (0, 2.27, 4.54, 6.81, 9.08, 11.35, 13.62, 15.89, 18.16, 20.43, 22.70 μg/mL) were transferred individually into a cuvette, fluorescence spectra were recorded with an Edinburgh FLS1000 fluorescence spectrophotometer ($\lambda_{ex}$ = 365 nm; Slits: 1.5 nm; $\lambda_{em}$ = 451 nm; Slits: 1.5 nm).

**Fluorescence Spectral testing of the CdSe/ZnS QDs@MPA.** 2.0 mL of the CdSe/ZnS QDs@MPA solutions (0, 1.60, 3.20, 4.80, 6.40, 8.00, 9.60, 11.20, 12.80, 14.40, 16.00 μg/mL) were transferred individually into a cuvette, fluorescence spectra were recorded with an Edinburgh FLS1000 fluorescence spectrophotometer ($\lambda_{ex}$ = 365 nm; Slits: 1.5 nm; $\lambda_{em}$ = 639 nm; Slits: 1.5 nm).

**Fluorescence Spectral testing of the CdSe/ZnS QDs@FNAC.** 2.0 mL of the CdSe/ZnS QDs@MPA solutions (0, 3.87, 7.74, 11.61, 15.48, 19.35, 23.22, 27.09, 30.96, 34.83, 38.70 μg/mL) were transferred individually into a cuvette, fluorescence spectra were recorded with an Edinburgh FLS1000 fluorescence spectrophotometer ($\lambda_{ex}$ = 365 nm; Slits: 1.5 nm; $\lambda_{em}$ = 639 nm; Slits: 1.5 nm).

### 1.3 Preparation and testing of $KMnO_4$ solution

**$KMnO_4$ stock solution (10 mM).** 79 mg of $KMnO_4$ solid was dissolved in 50 mL of deionized water to prepare the $KMnO_4$ stock solution with a concentration of 10 mM. Then the solution was diluted with deionized water to obtain various concentrations of $KMnO_4$ solutions.

**Sensing testing of the probe spectral performance.** $KMnO_4$ solution (1 mM, 200 μL) was added into 2.0 mL of the FNAC, CdSe/ZnS QDs@MPA, CdSe/ZnS QDs@FNAC solution in a cuvette, respectively. Fluorescence intensity was recorded with an Edinburgh FLS1000 fluorescence spectrophotometer ($\lambda_{ex}$ = 365 nm; Slits: 1.5 nm; Slits: 1.5 nm). The fluorescent images of the probe over time were recorded with iPhone 14.

**Spectral response testing of the FNAC.** 200 μL of $KMnO_4$ solutions (0, 10, 20, 40, 60, 80, 100, 150, 300, 500, 800, 1000 μM, respectively) were added into 2.0 mL of the FNAC solution (22.70 μg/mL) in a cuvette, respectively. Fluorescence detection performance of $KMnO_4$ was recorded with an Edinburgh FLS1000 fluorescence spectrophotometer ($\lambda_{ex}$ = 365 nm; Slits: 1.5 nm; $\lambda_{em}$ = 521 nm; Slits: 1.5 nm).

**Spectral response testing of the CdSe/ZnS QDs@MPA.** 200 μL of $KMnO_4$ solutions (0, 10, 20, 40, 60, 80, 100, 150, 300, 500, 800, 1000 μM, respectively) were added into 2.0 mL of the CdSe/ZnS QDs@MPA solution (16.00 μg/mL) in a cuvette, respectively. Fluorescence detection performance of $KMnO_4$ was recorded with an Edinburgh FLS1000 fluorescence spectrophotometer ($\lambda_{ex}$ = 365 nm; Slits: 1.5 nm; $\lambda_{em}$ = 639 nm; Slits: 1.5 nm).

**Spectral response testing of the CdSe/ZnS QDs@FNAC.** 200 μL of $KMnO_4$ solutions (0, 10, 20, 40, 60, 80, 100, 150, 300, 500, 800, 1000 μM, respectively) were added into 2.0 mL of the CdSe/ZnS QDs@FNAC solution (38.70 μg/mL) in a cuvette, respectively. Fluorescence detection performance of $KMnO_4$ was recorded with an Edinburgh FLS1000 fluorescence spectrophotometer ($\lambda_{ex}$ = 365 nm; Slits: 1.5 nm; $\lambda_{em}$ = 521 nm, 639 nm; Slits: 1.5 nm).

**Preparation and calculation process of the limit of detection (LOD) of the CdSe/ZnS QDs@FNAC.** The CdSe/ZnS QDs@FNAC was dissolved in 100 mL of $CH_3CN/H_2O$ mixed solvent with a volume ratio of 3:7, and then 200 μL of $H_2O$ was added into 2.0 mL of the CdSe/ZnS QDs@FNAC solution in a cuvette respectively to obtain 11 blank samples for CdSe/ZnS QDs@FNAC. The fluorescence spectra were recorded with an Edinburgh FLS1000 fluorescence spectrophotometer ($\lambda_{ex}$ = 365 nm; Slits: 1.5 nm).

The LOD of the CdSe/ZnS QDs@FNAC towards $KMnO_4$ is calculated by the following Equation:

$$LOD=3\sigma/k \quad \text{(Equation S1)}$$

where σ denotes the standard deviation of the CdSe/ZnS QDs@FNAC solution after 11 blank sample tests, k denotes the slope of the concentration versus intensity curve for the target analyte in Figure S7. The detailed calculation process is as follows:

**The LOD of the CdSe/ZnS QDs@FNAC towards $KMnO_4$.** σ is the standard deviation of the emission intensity ratio of the CdSe/ZnS QDs@FNAC solution at 521 nm and 639 nm after conducting 11 tests, and the value is calculated as 0.000085, k is 0.0531 as obtained in Figure S7, therefore, the LOD of the CdSe/ZnS QDs@FNAC solution towards $KMnO_4$ is $LOD=3\times0.000085/0.0531$ and the value is calculated as 4.80 nM.

### 1.4 Preparation and testing of trace analytes

**Analyte stock solutions (10 mM).** NaCl, KCl, $MgCl_2$, $CaCl_2$, $Na_2SO_4$, $NH_4Br$, sodium dodecyl sulfate (SDS), Urea, $Zn(Ac)_2$, KI, $Na_2SO_3$, $NaNO_2$, $NaClO_2$, $NaIO_3$, $NaBrO_3$, KBr, $KNO_3$, $NH_4NO_3$, $KClO_3$, $NaClO_4$, $H_2O_2$, NaClO, $Na_2S$ were dissolved in deionized water to prepare the analyte stock solutions with a concentration of 10 mM.

**Selectivity testing process.** The analyte stock solution was diluted to 1 mM, then the stock solution (1 mM, 200 μL) of certain analyte was added into a cuvette filled with 2.0 mL of the CdSe/ZnS QDs@FNAC solution. After the reaction, the fluorescence spectra and images were measured and recorded ($\lambda_{ex}$ = 365 nm; Slits: 1.5 nm; $\lambda_{em}$ = 520 nm, 639 nm; Slits: 1.5 nm; Spectrometer: Edinburgh FLS1000).

**Anti-interference testing process.** The mixture of the stock solution (10 mM, 100 μL) of certain analyte and $KMnO_4$ stock solution (2 mM, 100 μL) was added into a cuvette filled with 2.0 mL of the CdSe/ZnS QDs@FNAC solution. After the reaction, the fluorescence spectra and images were measured and recorded ($\lambda_{ex}$ = 365 nm; Slits: 1.5 nm; $\lambda_{em}$ = 520 nm, 639 nm; Slits: 1.5 nm; Spectrometer: Edinburgh FLS1000).

### 1.5 Testing of the CdSe/ZnS QDs@FNAC-based polyacrylamide hydrogel sensor for $KMnO_4$ particles detection

**Fluorescence sensing performance test of the sensor for $KMnO_4$ particles.** Different sizes of $KMnO_4$ particles were added to a sensor by spraying. Under irradiation with a 365 nm UV lamp, the sensing process was captured under a MERCURY GigE Camera (MER-2000-5GC), and the fluorescent images on the CdSe/ZnS QDs@FNAC-based polyacrylamide hydrogel sensor were recorded.

**Calculation of the size of $KMnO_4$ solid particles.** The diameters (d) of the solid $KMnO_4$ particles were determined by measuring the corresponding inter-distance from the initial frame (0 s) captured in the video. The mass (m) of individual $KMnO_4$ solid particles was then calculated using the following formula:

$$m = \frac{4}{3}\rho\pi(\frac{d}{2})^3 \qquad (1)$$

where ρ corresponds to the density of solid $KMnO_4$, which is 2.7 g/cm$^3$.

### 1.6 Preparation and testing of the sensing chip for $KMnO_4$ particles detection

**Preparation of polyacrylamide hydrogel sensor.** 1.4 g of acrylamide (AAm, 19.7 mmol), 10.0 mg of N,N'-methylene diacrylamide (MBA, 64.8 μmol), 9.0 mg of azobisisobutyronitrile (AIBN, 54.8 μmol), 10 mL of deionized water were thoroughly mixed in a 50 mL flask. The mixture was stirred at 520 rpm at room temperature for 2 h, then the mixture was transferred to a glass mold and incubated at 60 °C for 3 h to initiate polymerization.

Region 1. 1.51 mg chemodosimeter PA-TCF was dissolved in 0.5 L of THF solution to get the PA-TCF chemodosimeter solution (10 μM), then the obtained polyacrylamide hydrogel was cut into 0.5×0.5 cm squares and immersed in 200 μL of the aforementioned solution.

**Region 2.** The obtained polyacrylamide hydrogel was cut into 0.5×0.5 cm squares and immersed in 200 μL of FNAC solution (22.70 μg/mL).

**Region 3.** Obtained from the CdSe/ZnS QDs@FNAC-based polyacrylamide hydrogel sensor.

**Region 4.** The obtained polyacrylamide hydrogel was cut into 0.5×0.5 cm squares and immersed in 200 μL of the CdSe/ZnS QDs@MPA solution (16.00 μg/mL)

**Region 5.** 10 mg (E)-2-(3-cyano-4(4-(dimethylamino)styryl)-5,5-dimethylfuran-2(5H)-ylidene) malononitrile (DMA-CN) was dissolved in 3.78 L of THF/DMSO solution with a volume ratio of 5:25 to get the DMA-CN probe solution (8 μM). Then the obtained polyacrylamide hydrogel was cut into 0.5×0.5 cm squares and immersed in 200 μL of the aforementioned solution.

**Parameter Settings for the Logical Discrimination Flowchart.** The parameterization of HSV thresholds and MNCPP was synergistically optimized by considering the intrinsic optical properties of the system, hardware specifications, and empirical validation. Specifically, the HSV model was preferentially adopted over RGB due to its superior resilience to illumination and exposure variations. The hue range (H, 110–150) was precisely calibrated to match the 521 nm green emission of FNOH, while a saturation (S, >180) was applied to effectively sequester hydrogel autofluorescence. Furthermore, the Value range (V, 16–255) ensures robust sensitivity for $KMnO_4$ detection while obviating overexposure artifacts. In addition, an MNCPP threshold (>20) was implemented to suppress stochastic electronic noise, thereby ensuring the morphological integrity and accurate identification of the smallest target particles.

## 2. Calculation Method

All geometric structure optimization tasks of computational models related to QDs were performed using the CP2K 2023.1 package[1], which employs a mixed Gaussian and plane-wave (GPW) basis set. An energy cutoff of 400 Ry and a relative energy cutoff of 55 Ry were determined to be sufficient for achieving energy convergence. When optimizing the structure of the QDs anchored ligands, the model was treated as a low-dimensional system without periodic boundary conditions. A cubic simulation box (33.75 Å × 33.75Å × 33.75 Å) was constructed by expanding 7.5 Å outward from the boundary of the ligand-anchored QD system to form a vacuum region.

All ground-state ($S_0$) geometric structure were fully optimized using the Gaussian 16 program[2] with PBE0[3, 4] exchange-correlation functional combined with Grimme's DFT-D3(BJ)[5] empirical dispersion correction (abbreviated as PBE0-D3(BJ)). The 6-311G(d,p)[6, 7] basis set was employed for all atoms. To investigate vertical emission energies, the structures of the lowest singlet excited state ($S_1$) were optimized via time-dependent density functional theory (TD-DFT)[8] at PBE0-D3(BJ)/6-311G(d,p) level. Frequency calculations were further performed at the same theoretical level for the optimized geometries to confirm that all stationary points were true minimal (i.e., no imaginary frequencies). Then, the vertical absorption energies were determined based on the optimized $S_0$ structures using TD-DFT at the same level, considering the first 40 singlet excited states. The vertical emission energies were calculated as the vertical deexcitation energies based on the optimized lowest excited-state ($S_1$) structures, with the first three singlet−singlet electronic transitions ($S_1 \rightarrow S_0$) computed via TD-DFT. All Natural Transition Orbital (NTO) data were extracted from the original computational output files. The transition density matrices were subsequently decomposed into NTO pairs utilizing the Multiwfn

software package. Solvent effects were incorporated using the solvation model density (SMD)[9] with a $CH_3CN$:$H_2O$ (3:7, v/v) solvent mixture. Additionally, electrostatic potential diagrams given reaction site parameters, frontier molecular orbitals (FMOs) of the specific excited states, hydrogen bonding interactions analyzed via the independent gradient model (IGM)[10, 11] and atoms in molecules (AIM) theory, hole-electron analysis[12], quantitative examination of electrostatic potential surfaces[13] as well as the generation of various visual iso-surfaces or plane maps were obtained using the Multiwfn[14] program package, with visualization rendered via the VMD[15] software.

## 3. Supporting Schemes

$MnO_4^- + 8H^+ + 5e^- \rightarrow Mn^{2+} + 4\ H_2O$ ( + 1.51 V, in strong acid condition)

$MnO_4^- + 4H^+ + 3e^- \rightarrow MnO_2 + 4\ H_2O$ ( + 1.70 V, in acid~neutral condition)

$MnO_4^- + 2H_2O + 3e^- \rightarrow MnO_2 + 4\ OH^-$ ( + 0.59 V, in alkaline condition)

**Scheme S1.** The oxidative reactivity of $KMnO_4$ under different pH conditions[16].

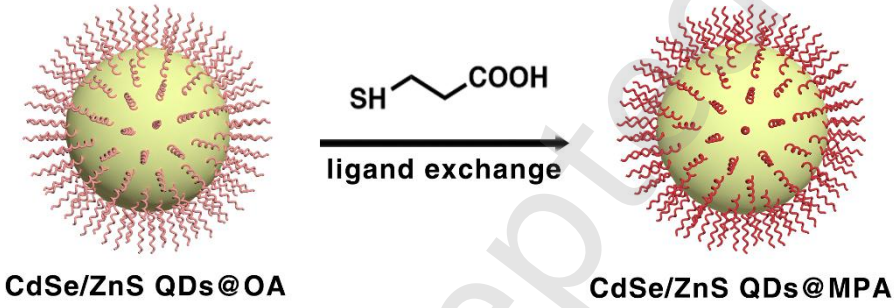


**Scheme S2**. Synthetic procedure of CdSe/ZnS QDs@MPA.

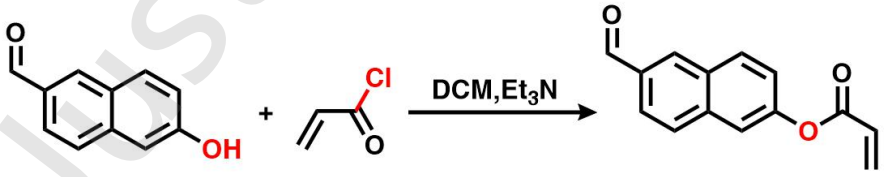


**Scheme S3**. Synthetic procedure of the probe molecule FNAC.

## 4. Supporting Figures

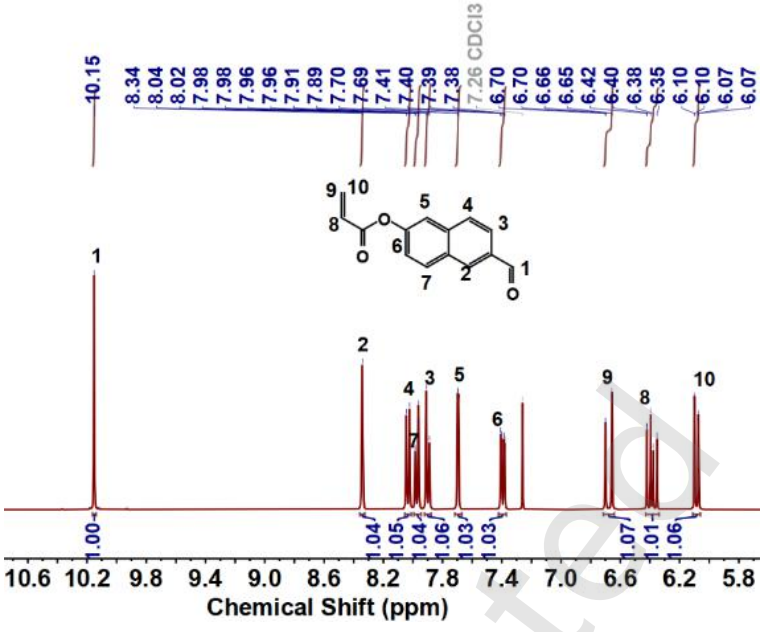


**Figure S1.** $^{1}$H NMR spectrum of the probe molecule FNAC ($CDCl_3$-*d*, 400 MHz).

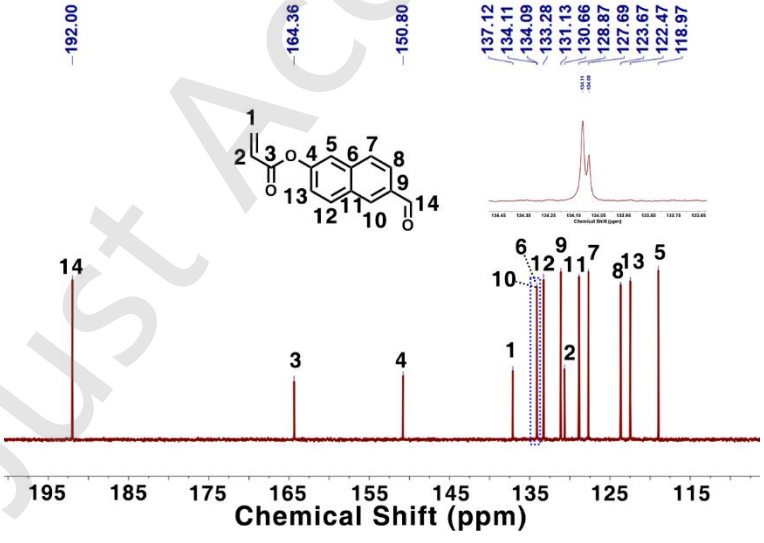


**Figure S2.** $^{13}$C NMR spectrum of the probe molecule FNAC ($CDCl_3$-*d*, 101 MHz).

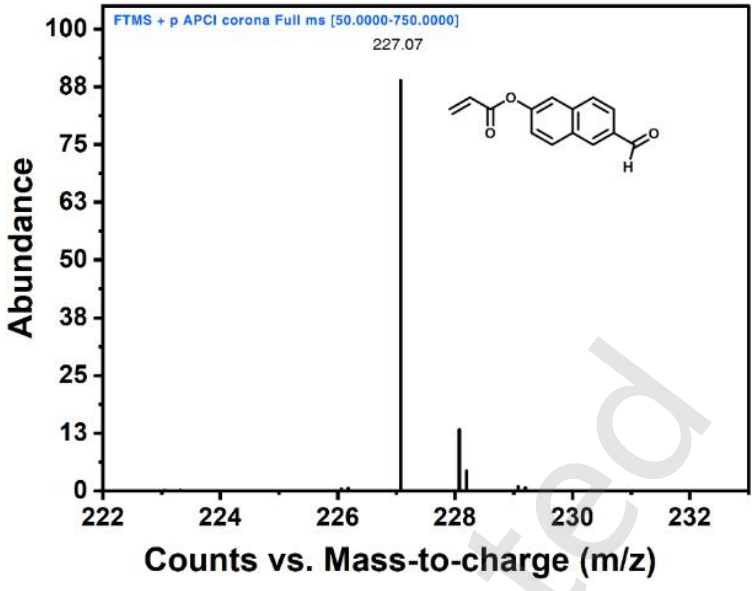


**Figure S3.** HRMS spectrum of the probe molecule FNAC.

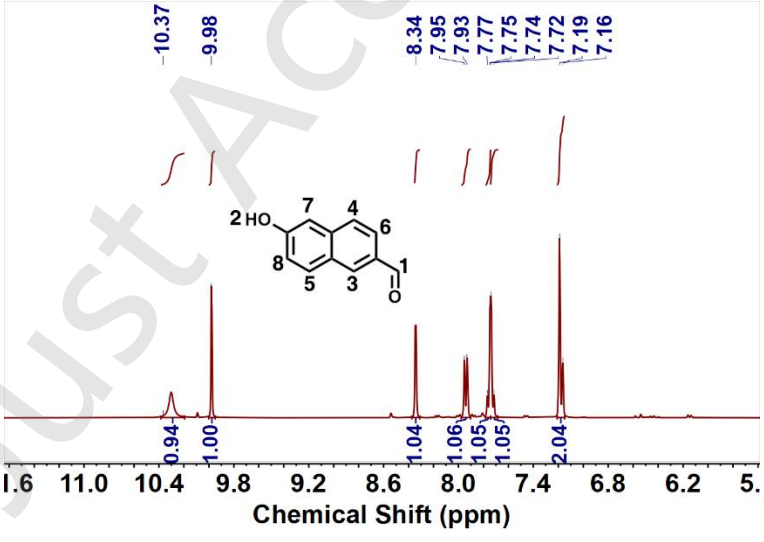


**Figure S4.** $^{1}$H NMR spectrum of the reaction product FNOH ($CDCl_3$-*d*, 400 MHz).

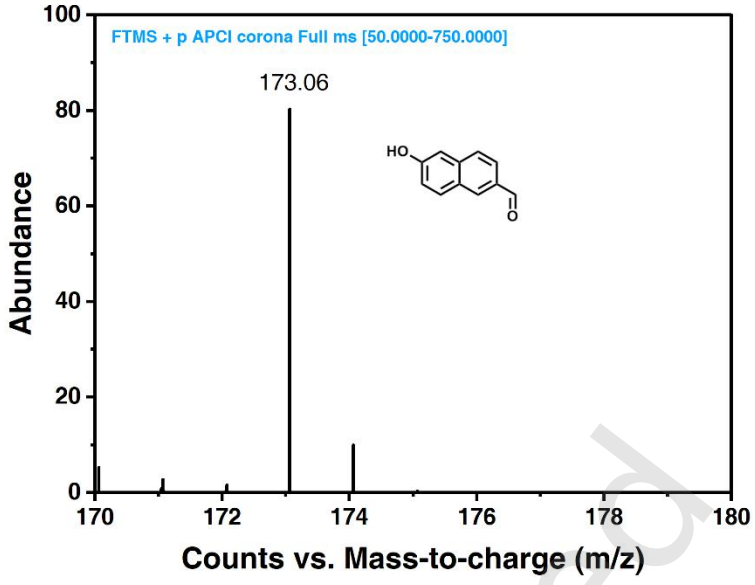


**Figure S5.** HRMS spectrum of the reaction product FNOH.

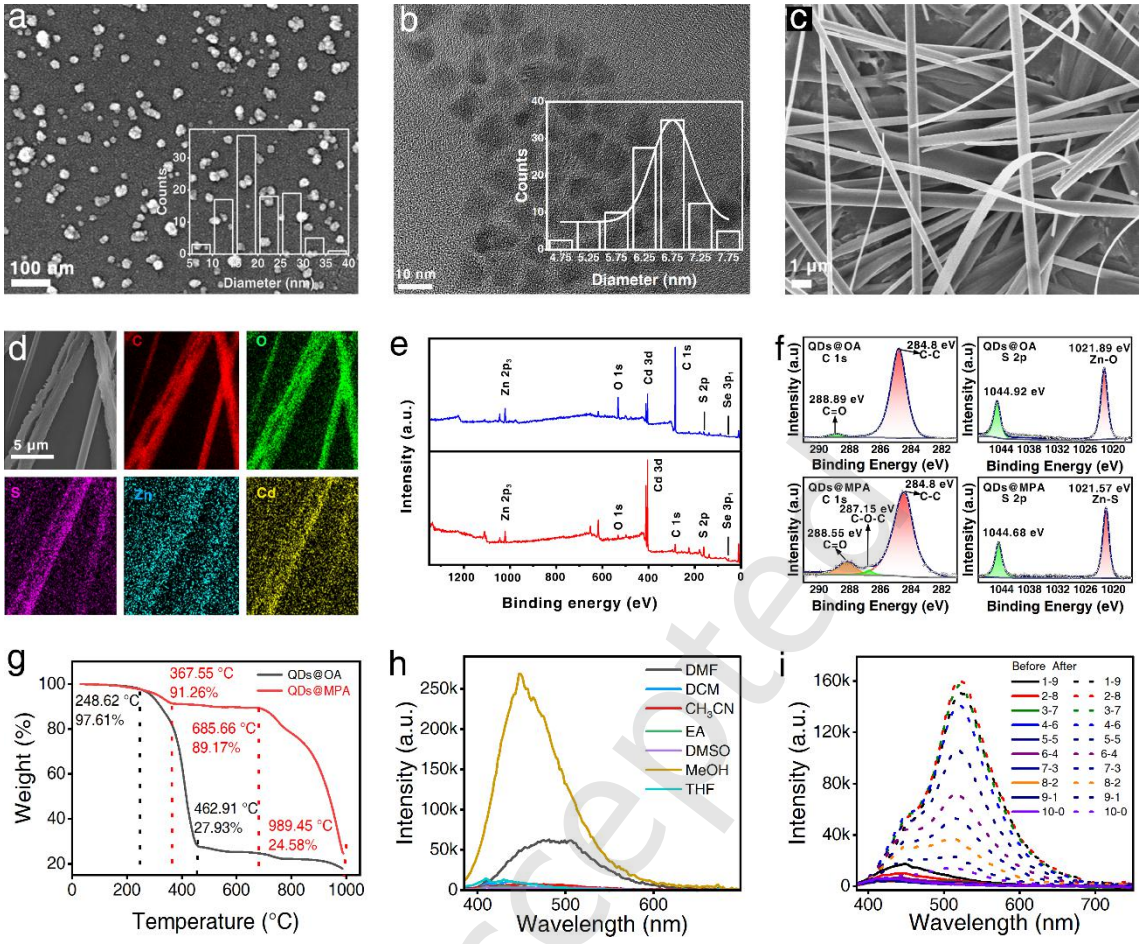


**Figure S6.** (a) Transmission Electron Microscopy (TEM) image and corresponding lateral size distribution of CdSe/ZnS QDs@OA. (b) Scanning electron microscope (SEM) image and corresponding lateral size distribution of CdSe/ZnS QDs@MPA. (c) SEM image of FNAC. (d) SEM image and the corresponding energy-dispersive spectroscopy (EDS) mappings of C, O S, Zn, and Cd elements of CdSe/ZnS QDs@FNAC. (e) Full-scan X-ray photoelectron spectroscopy (XPS) of CdSe/ZnS QDs@OA and CdSe/ZnS QDs@MPA. (f) The C 1s and Zn 2p XPS of CdSe/ZnS QDs@OA and CdSe/ZnS QDs@MPA. (g) TGA curves of CdSe/ZnS QDs@OA and CdSe/ZnS QDs@MPA obtained at a heating rate of 5 K/min. Fluorescence spectra of the FNAC (h) in different solvents, and (i) in $CH_3CN$ with different water content before and after detecting $KMnO_4$.

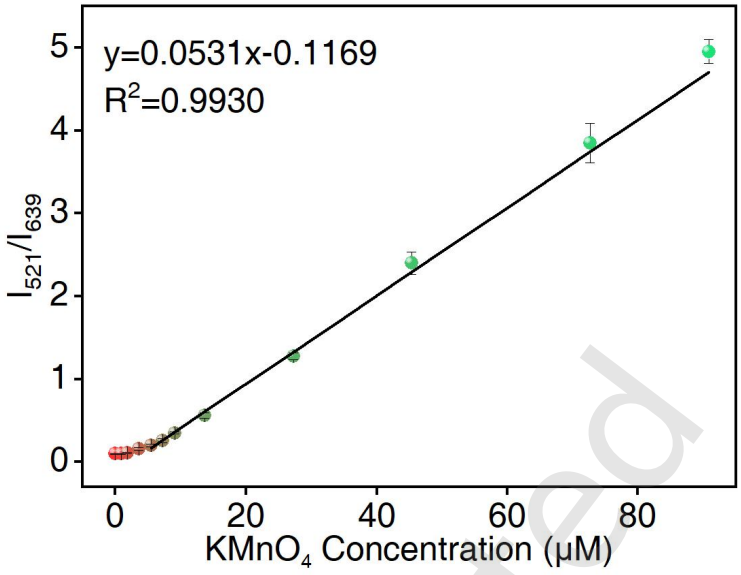


**Figure S7.** Emission intensity ratio ($I_{521}/I_{639}$) as a function of $KMnO_4$ concentration.

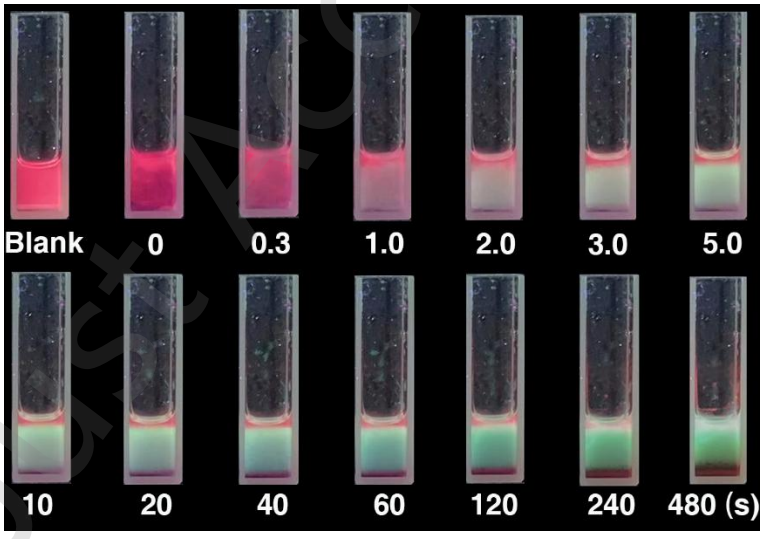


**Figure S8.** Time-lapse images extracted from the videos of CdSe/ZnS QDs@FNAC detecting $KMnO_4$ captured using a digital camera (0-480 s).

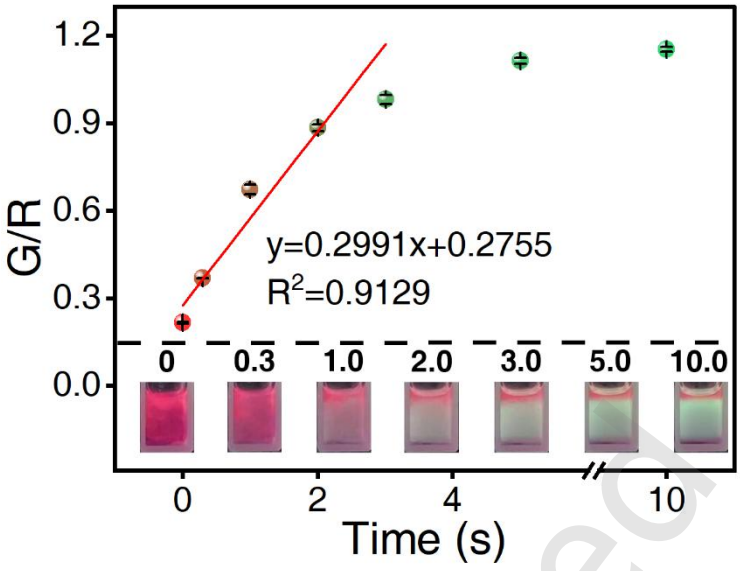


**Figure S9.** Time-dependent curves of G/R values extracted from Time-lapse images, which captured from a video of CdSe/ZnS QDs@FNAC detecting $KMnO_4$ *via* a digital camera.

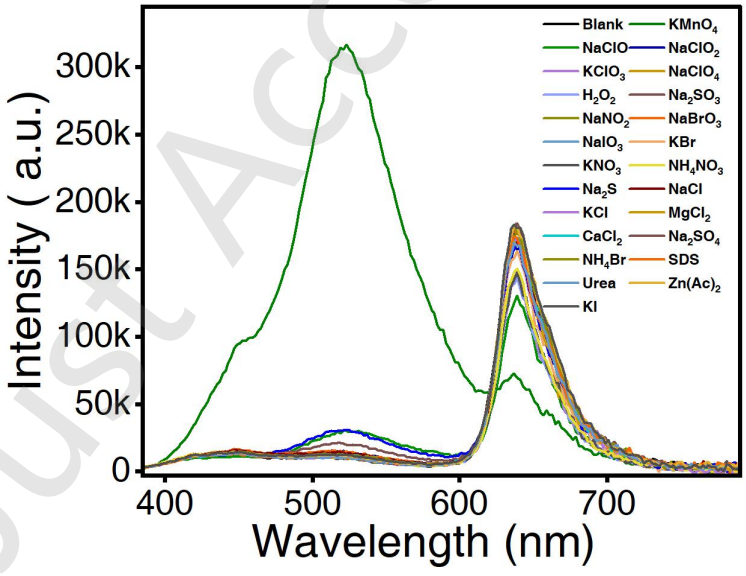


**Figure S10.** The selectivity of CdSe/ZnS QDs@FNAC towards $KMnO_4$. Fluorescence emission spectra of CdSe/ZnS QDs@FNAC in the presence of various test analytes solution with a concentration of 1 mM (the spectra were repeated for three times).

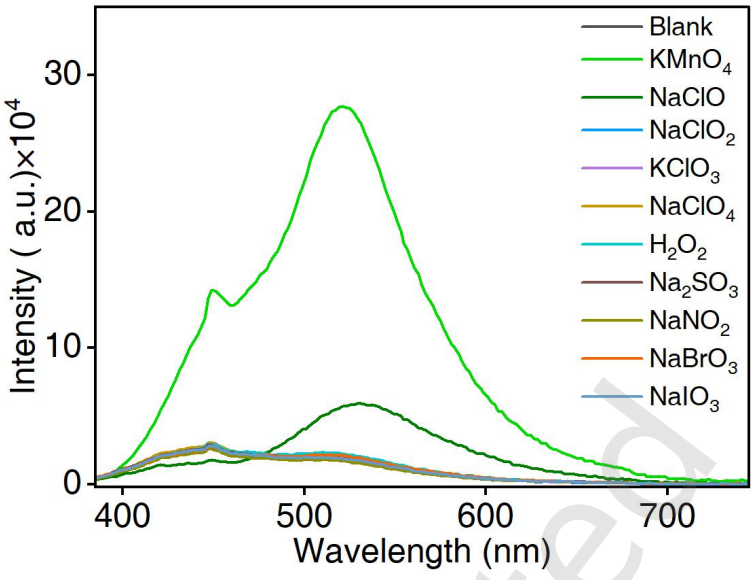


**Figure S11.** Fluorescence emission spectra of FNAC in the presence of various analytes at a concentration of 1 mM (the spectra were repeated for three times).

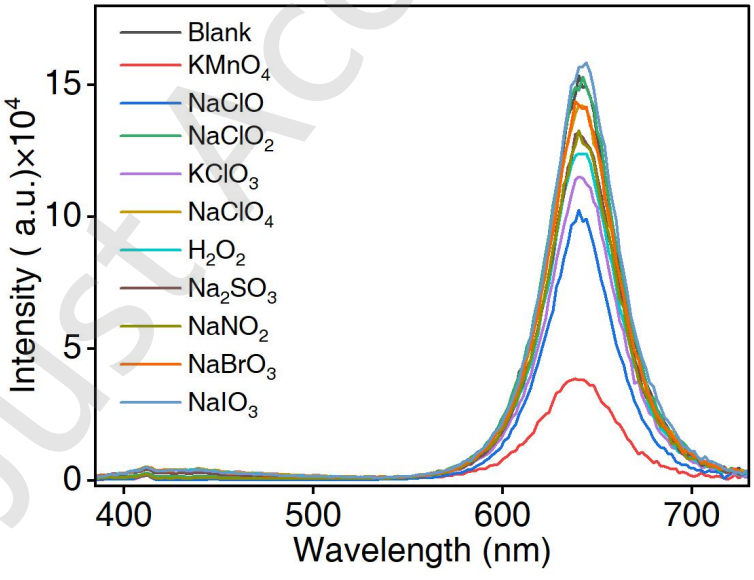


**Figure S12.** Fluorescence emission spectra of CdSe/ZnS QDs@MPA in the presence of various analytes at a concentration of 1 mM (the spectra were repeated for three times).

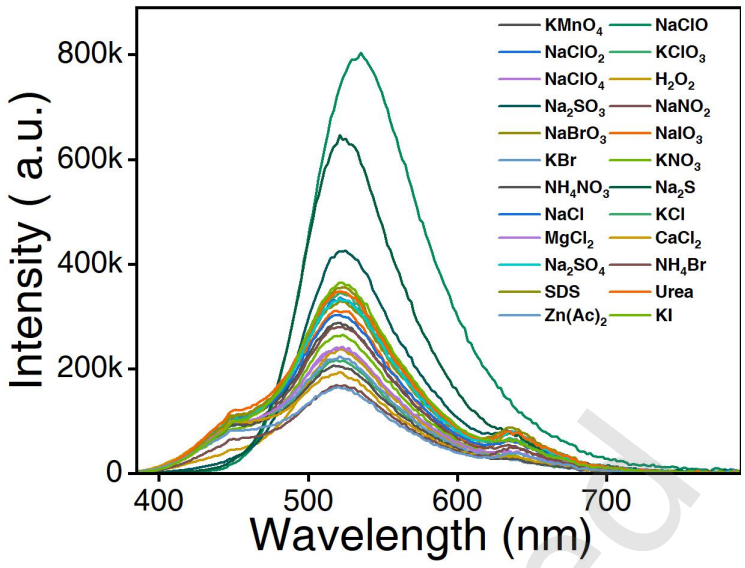


**Figure S13.** The anti-interference of CdSe/ZnS QDs@FNAC towards $KMnO_4$. Fluorescence emission spectra of CdSe/ZnS QDs@FNAC in the presence of a mixture solution of various interferents (10 mM) and $KMnO_4$ (1 mM) (the spectra were repeated for three times).

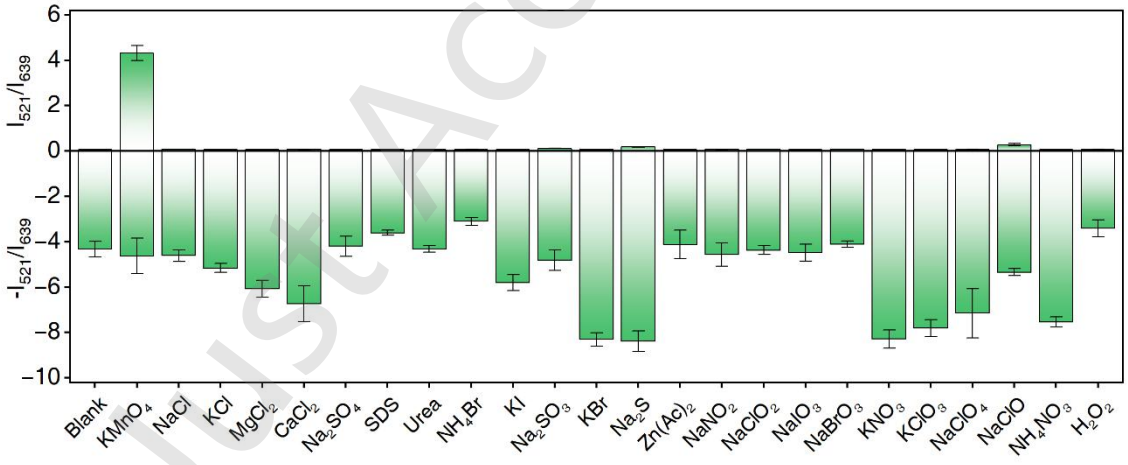


**Figure S14.** Histogram of the intensity ratio of $I_{521}/I_{639}$ in response to various interferents (1 mM) and $KMnO_4$ (1 mM), and a mixture of $KMnO_4$ (1 mM) with each interferent (10 mM), respectively. Note that the excitation wavelength is 365 nm, and the standard deviations were obtained from three repeated measurements.

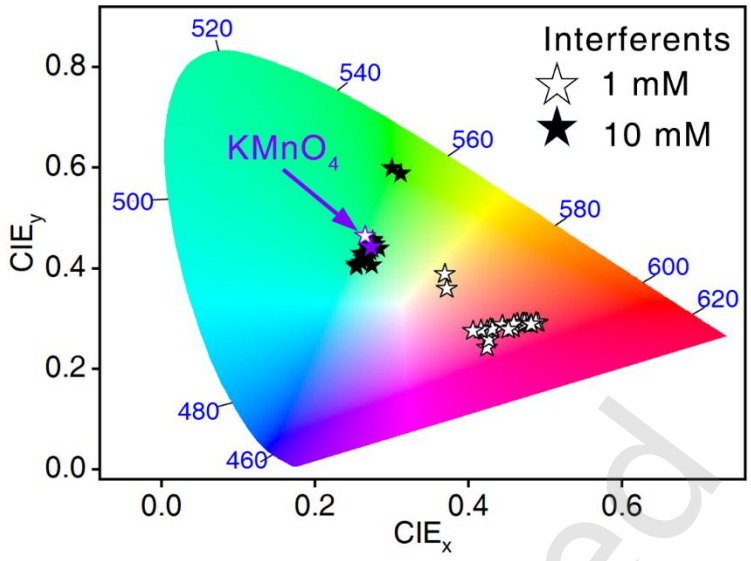


**Figure S15.** The specificity and anti-interference evaluation of CdSe/ZnS QDs@FNAC based on the CIE 1931 chromaticity diagram. Note that the excitation wavelength is 365 nm, and the standard deviations were obtained from three repeated measurements.

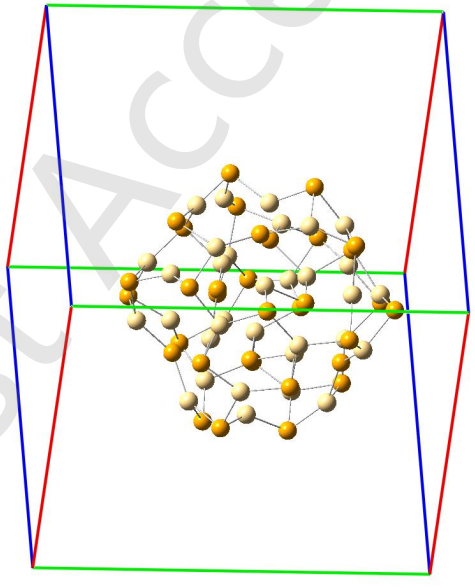

**Figure S16.** The computational model of $Cd_{33}Se_{33}$ QDs.

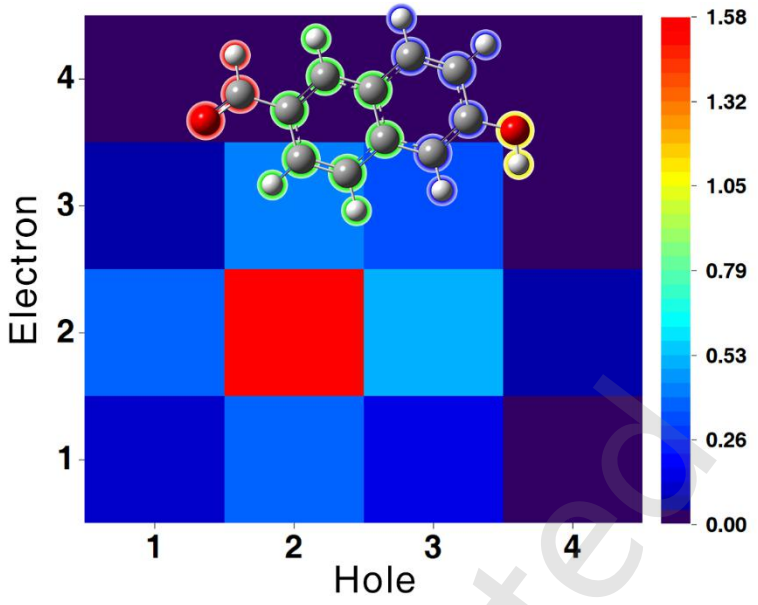


**Figure S17.** The fragment transition density matrix maps of FNOH.

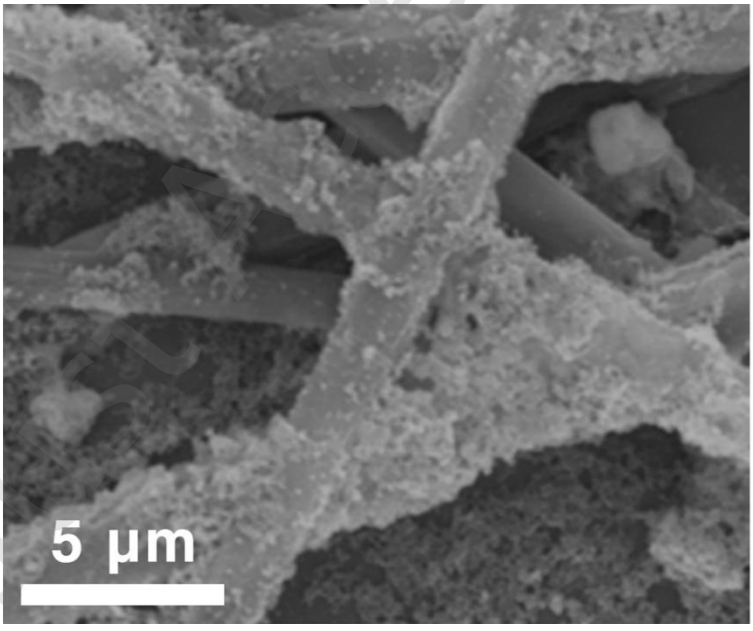


**Figure S18.** SEM image of CdSe/ZnS QDs@FNAC after detection of $KMnO_4$.

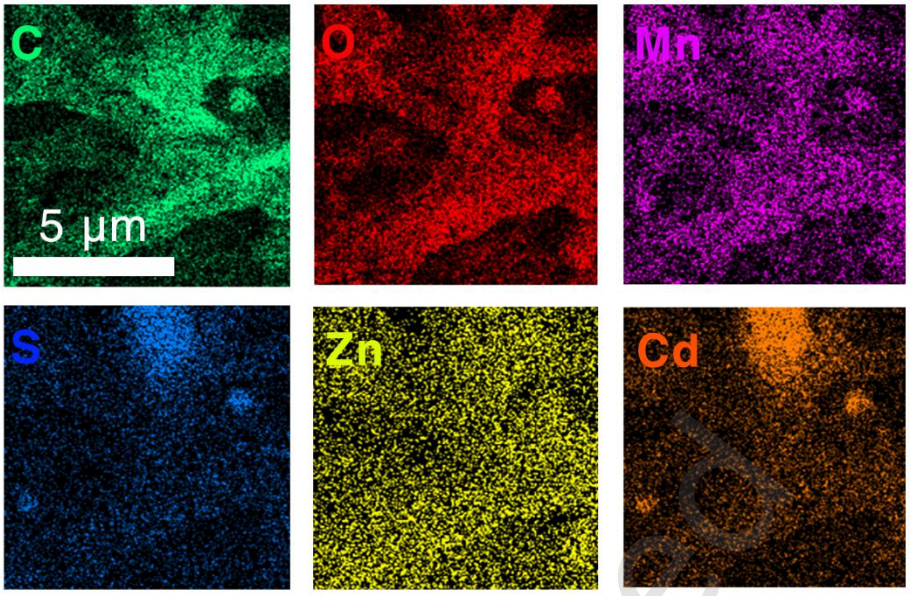


**Figure S19.** EDS mappings of C, O, Mn, S, Zn and Cd of CdSe/ZnS QDs@FNAC after detection of $KMnO_4$.

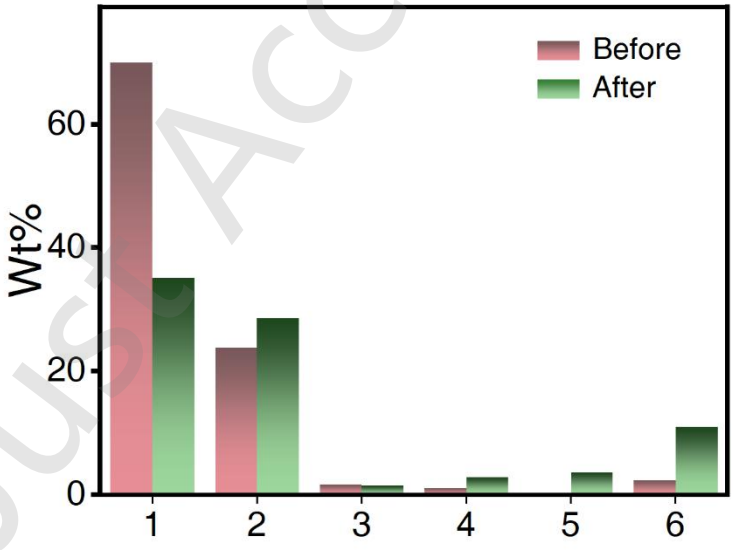


**Figure S20.** Comparison of elemental mass contents of C, O, S, Zn, Se and Cd in CdSe/ZnS QDs@FNAC before and after reaction with $KMnO_4$.

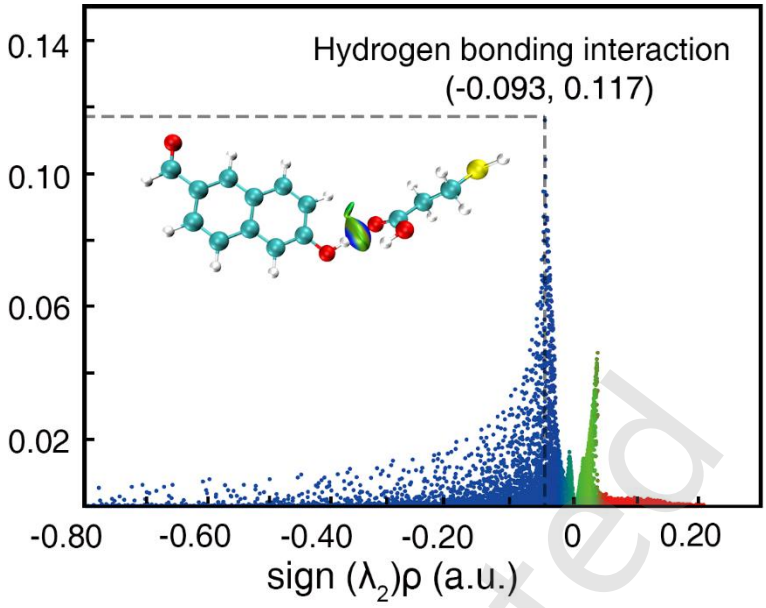


**Figure S21.** Isosurface (value=0.01 a.u.) and scatter graph of noncovalent interactions between the functional carrier CdSe/ZnS QDs@MPA and the product FNOH.

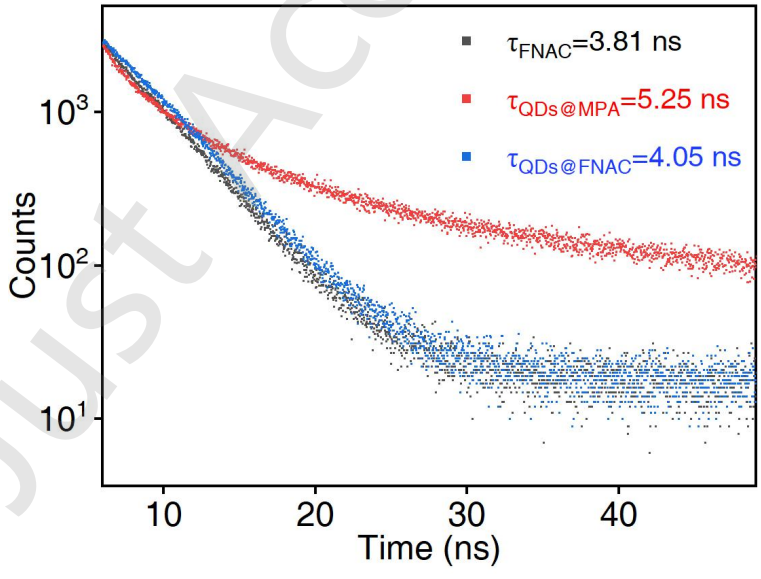


**Figure S22.** The fluorescence lifetime spectra of FNAC, CdSe/ZnS QDs@MPA, and CdSe/ZnS QDs@FNAC after reaction with $KMnO_4$.

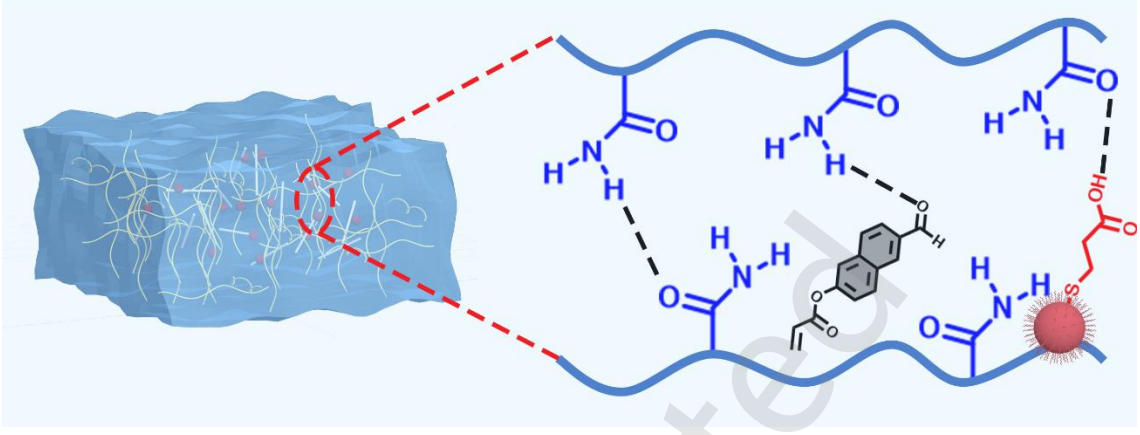

**Figure S23.** Schematic diagram of the interaction between the CdSe/ZnS QDs@FNAC and PAM hydrogel.

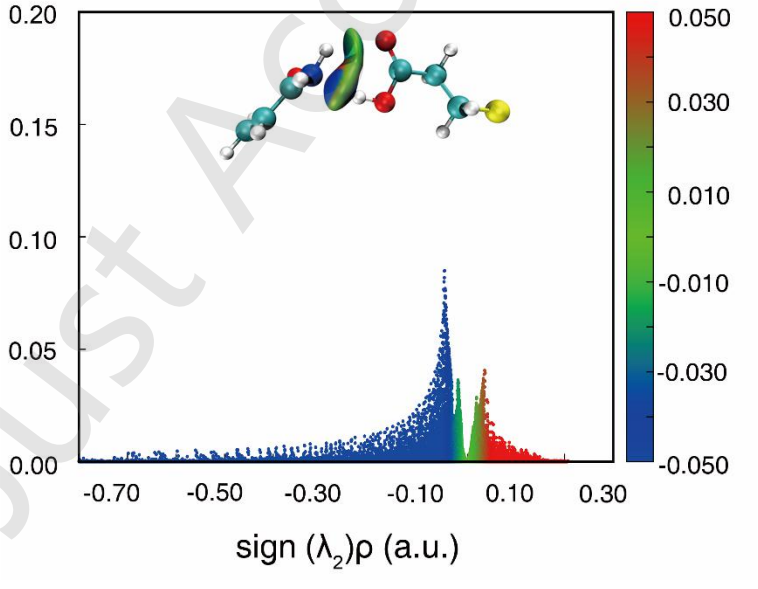


**Figure S24.** Isosurface (value=0.01 a.u.) and scatter graph of noncovalent interactions between PAM hydrogel unit and CdSe/ZnS QDs@FNAC.

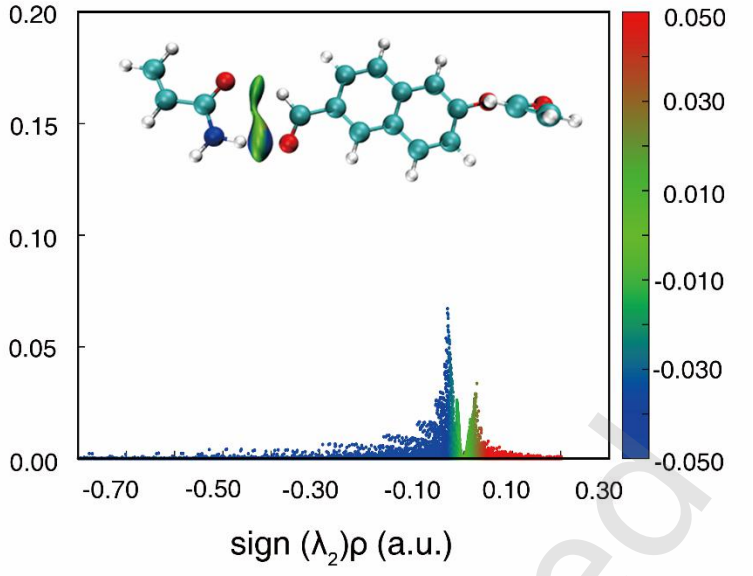


**Figure S25.** Isosurface (value=0.01 a.u.) and scatter graph of noncovalent interactions between PAM hydrogel unit and FNOH.

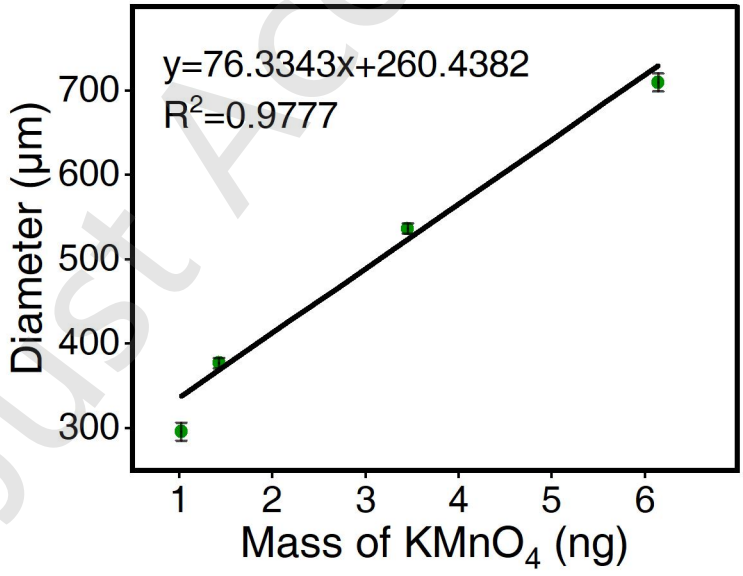


**Figure S26.** Relationship between the diffusion diameter at 15 s and the mass of the $KMnO_4$ particles.

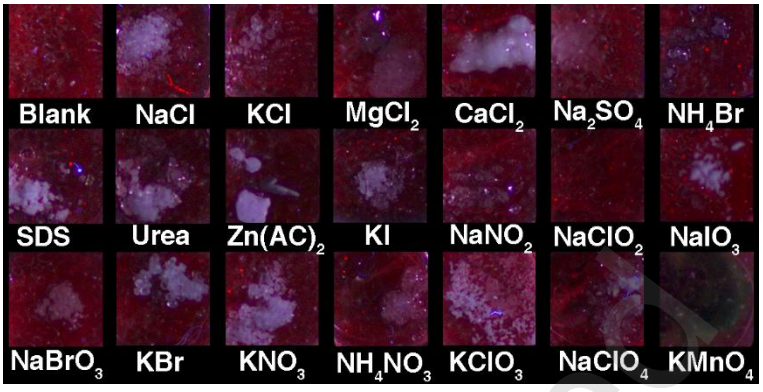


**Figure S27.** Selective fluorescence images of the CdSe/ZnS QDs@FNAC-embedded hydrogel sensing chip.

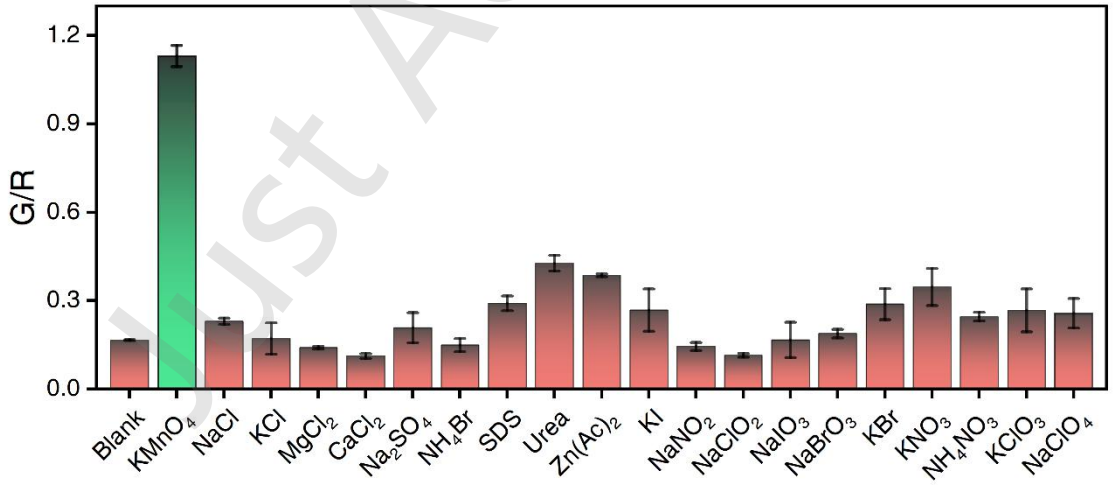


**Figure S28.** Selectivity of the hydrogel sensor toward 19 kinds of interferents.

## 5. Supporting Tables

**Table S1.** The element content of CdSe/ZnS QDs@FNAC before and after reaction with $KMnO_4$.

| Element | Wt (%) | |
|---|---|---|
| | **Before** | **After** |
| C | 70.81 | 35.11 |
| O | 24.06 | 28.59 |
| S | 1.63 | 1.48 |
| Zn | 1.13 | 2.80 |
| Se | 0 | 3.63 |
| Cd | 2.37 | 11 |
| Mn | 0 | 15.98 |
| K | 0 | 1.41 |
| Total | 100 | 100 |

**Table S2.** Comparison of the recently developed optical methods for the detection of $KMnO_4$.

| Materials | Detection Mechanism | Detection Mode | Limit of Detection (LOD) | Minimum Detectable Particle Mass | Response Time (s) | Ref. |
|---|---|---|---|---|---|---|
| Eu(III)-functionalized in-MOF | Competition of energy | Turn off | 62.84 μM | / | 300 s | [17] |
| Dye-CDs@MOFs | IFE | Turn off | 0.08 μM | / | 1800 s | [18] |
| Zinc(II)-organic framework | IFE | Turn off | 0.27 μM | / | 30 s | [19] |
| Naphthalene nanoparticles (NTNPs) | Electron transfer | Turn on | 759.49 nM | / | - | [20] |
| GNPs@Ag core-shell nanoparticle | Oxidation effect | Colorimetric | 46 nM | / | 300 s | [21] |
| UCNS/TMB nanosystem | IFE | Turn off | 0.243 μM | / | 120 s | [22] |
| Water soluble oligomer | IFE | Turn off | 0.392 μM | / | 1800 s | [23] |
| N,P-Dual-doped carbon dots | IFE | Turn off | 48.3 nM | / | 40 s | [24] |
| Zn(all-bdc)(Py) MOF | IFE | Turn off | 0.13 μM | / | / | [25] |
| [Zr6O4(OH)4(PVDC)6]4·66DMF | PET | Turn on | 14.8 μM | / | 360 s | [26] |
| **CdSe/ZnS QDs@FNAC** | **PET** | **Ratiometric fluorescence** | 4.80 nM | **1.08 ng** | **<1 s** | **This work** |

**Table S3.** The main physical parameters of FNAC, $Cd_{33}Se_{33}$ QDs@3MPA, $Cd_{33}Se_{33}$ QDs and FNOH calculated at the PBE0-D3(BJ)/6-31G(d,p) level.

| | HOMO (eV) | LUMO (eV) | Gap (eV) | D (Å) | Sr (a.u.) | t (Å) |
|---|---|---|---|---|---|---|
| FNAC | -6.61 | -1.94 | 4.67 | 1.16 | 0.7386 | -1.08 |
| $Cd_{33}Se_{33}$ QDs@3MPA | -5.61 | -3.68 | 1.93 | 10.37 | 0.0811 | 8.41 |
| $Cd_{33}Se_{33}$ QDs | -6.65 | -3.46 | 3.19 | 5.32 | 0.3796 | 2.56 |
| FNOH | -6.27 | -1.67 | 4.60 | 2.05 | 0.7370 | -0.15 |

**Table S4.** Natural Transition Orbital (NTO) analysis for the vertical emission ($S_1 \gamma S_0$) of the optimized excited state structure of $Cd_{33}Se_{33}$ QDs@3MPA.

| Contribution Rank | Hole Orbital (Occupied NTO) | Electron Orbital (Unoccupied NTO) | Eigenvalue (λ) | Contribution Percentage (%) |
|---|---|---|---|---|
| 1 | $MO^{975}$ | $MO^{976}$ | 0.999930 | 99.9955 |
| 2 | $MO^{974}$ | $MO^{977}$ | 0.000023 | 0.0023 |
| 3 | $MO^{973}$ | $MO^{978}$ | 0.000015 | 0.0015 |
| 4 | $MO^{972}$ | $MO^{979}$ | 0.000004 | 0.0004 |
| 5 | $MO^{971}$ | $MO^{980}$ | 0.000003 | 0.0003 |

**Note:** Molecular orbitals $MO^{975}$ and $MO^{976}$ are identified as the Highest Occupied Molecular Orbital (HOMO) and Lowest Unoccupied Molecular Orbital (LUMO), respectively. The percentage contribution of each NTO is defined as the ratio of its corresponding eigenvalue to the sum of all eigenvalues.

# References


[1] Kühne, T. D.; Iannuzzi, M.; Del Ben, M.; Rybkin, V. V.; Seewald, P.; Stein, F.; Laino, T.; Khaliullin, R. Z.; Schütt, O.; Schiffmann, F.; Golze, D.; Wilhelm, J.; Chulkov, S.; Bani-Hashemian, M. H.; Weber, V.; Borštnik, U.; Taillefumier, M.; Jakobovits, A. S.; Lazzaro, A.; Pabst, H.; Müller, T.; Schade, R.; Guidon, M.; Andermatt, S.; Holmberg, N.; Schenter, G. K.; Hehn, A.; Bussy, A.; Belleflamme, F.; Tabacchi, G.; Glöß, A.; Lass, M.; Bethune, I.; Mundy, C. J.; Plessl, C.; Watkins, M.; VandeVondele, J.; Krack, M.; Hutter, J. Cp2k: An Electronic Structure and Molecular Dynamics Software Package - Quickstep: Efficient and Accurate Electronic Structure Calculations. *J. Chem. Phys.* **2020**, 152, 194103-104150.

[2] Frisch, M. J.; Trucks, G. W.; Schlegel, H. B.; Scuseria, G. E.; Robb, M. A.; Cheeseman, J. R.; Scalmani, G.; Barone, V.; Petersson, G. A.; Nakatsuji, H.; Li, X.; Caricato, M.; Marenich, A. V.; Bloino, J.; Janesko, B. G.; Gomperts, R.; Mennucci, B.; Hratchian, H. P.; Ortiz, J. V.; Izmaylov, A. F.; Sonnenberg, J. L.; Williams; Ding, F.; Lipparini, F.; Egidi, F.; Goings, J.; Peng, B.; Petrone, A.; Henderson, T.; Ranasinghe, D.; Zakrzewski, V. G.; Gao, J.; Rega, N.; Zheng, G.; Liang, W.; Hada, M.; Ehara, M.; Toyota, K.; Fukuda, R.; Hasegawa, J.; Ishida, M.; Nakajima, T.; Honda, Y.; Kitao, O.; Nakai, H.; Vreven, T.; Throssell, K.; Montgomery Jr., J. A.; Peralta, J. E.; Ogliaro, F.; Bearpark, M. J.; Heyd, J. J.; Brothers, E. N.; Kudin, K. N.; Staroverov, V. N.; Keith, T. A.; Kobayashi, R.; Normand, J.; Raghavachari, K.; Rendell, A. P.; Burant, J. C.; Iyengar, S. S.; Tomasi, J.; Cossi, M.; Millam, J. M.; Klene, M.; Adamo, C.; Cammi, R.; Ochterski, J. W.; Martin, R. L.; Morokuma, K.; Farkas, O.; Foresman, J. B.; Fox, D. J. *Gaussian 16 Rev. C.01*; 2016.

[3] Grimme, S. Density Functional Theory with London Dispersion Corrections. *WIREs Comput. Mol. Sci.* **2011**, 1, 211–228.

[4] Grimme, S.; Ehrlich, S.; Goerigk, L. Effect of the Damping Function in Dispersion Corrected Density Functional Theory. *J. Comput. Chem.* **2011**, 32, 1456–1465.

[5] Parr, R. G. G., S. R.; Bartolotti, L. J. Local Density Functional Theory of Atoms and Molecules. *Proceedings of the National Academy of Sciences of the United States of America* **1979**, 76, 2522–2526.

[6] Hehre, W. J.; Ditchfield, R.; Pople, J. A. Self-Consistent Molecular Orbital Methods. Xii. Further Extensions of Gaussian-Type Basis Sets for Use in Molecular Orbital Studies of Organic Molecules. *J. Chem. Phys.* **1972**, 56, 2257–2262.

[7] Pople, P. C. H. a. J. A. The Influence of Polarization Functions on Molecular Orbital Hydrogenation Energies. *Theor. Chim. Acta* **1973**, 28, 213–222.

[8] Barone, G. S. M. J. F. B. M. J. T. R. C. V. Geometries and Properties of Excited States in the Gas Phase and in Solution: Theory and Application of a Time-Dependent Density Functional Theory Polarizable Continuum Model *J. Chem. Phys.* **2006**, 124, 094107.

[9] Aleksandr V. Marenich, C. J. C., and Donald G. Truhlar. Universal Solvation Model Based on Solute Electron Density and on a Continuum Model of the Solvent Defined by the Bulk Dielectric Constant and Atomic Surface Tensions. *J. Phys. Chem. B* **2009**, 113, 6378.

[10] Lu, T.; Chen, Q. Independent Gradient Model Based on Hirshfeld Partition: A New Method for Visual Study of Interactions in Chemical Systems. *J. Comput. Chem.* **2022**, 43, 539–555.

[11] Lefebvre, C.; Rubez, G.; Khartabil, H.; Boisson, J.; ContrerasGarcía, J.; Hénon, E. Accurately Extracting the Signature of Intermolecular Interactions Present in the NCI Plot of the Reduced Density Gradient Versus Electron Density. *Phys. Chem. Chem. Phys.* **2017**, 19, 17928–17936.

[12] Liu, Z.; Lu, T.; Chen, Q. An sp-Hybridized All-Carboatomic Ring, Cyclo [18] Carbon: Electronic Structure, Electronic Spectrum, and Optical Nonlinearity. *Carbon* **2020**, 165, 461–467.

[13] Lu, T.; Chen, F. Quantitative Analysis of Molecular Surface Based on Improved Marching Tetrahedra Algorithm. *J. Mol. Graphics Modell.* **2012**, 38, 314–323.

[14] Lu, T.; Chen, F. Multiwfn: A Multifunctional Wavefunction Analyzer. *J. Comput. Chem.* **2011**, 33, 580–592.

[15] Humphrey, W. D., A.; Schulten, K. Schulten, K. Vmd: Visual Molecular Dynamics. *J. Mol. Graphics Modell* **1996**, 14, 33.

[16] Wang, Y.; Zheng, K.; Guo, H.; Tian, L.; He, Y.; Wang, X.; Zhu, T.; Sun, P.; Liu, Y. Potassium Permanganate-Based Advanced Oxidation Processes for Wastewater Decontamination and Sludge Treatment: A Review. *Chem. Eng. J.* **2023**, 452, 139529-139545.

[17] Wu, J.-X.; Yan, B. Eu(III)-Functionalized In-MOF (In(OH)bpydc) as Fluorescent Probe for Highly Selectively Sensing Organic Small Molecules and Anions Especially for $CHCl_3$ and $MnO_4^-$. *J. Colloid Interface Sci.* **2017**, 504, 197–205.

[18] Zhu, K.; Fan, R.; Zheng, X.; Wang, P.; Chen, W.; Sun, T.; Gai, S.; Zhou, X.; Yang, Y. Dual-Emitting Dye-CdS@MOFs for Selective and Sensitive Identification of Antibiotics and $MnO_4^-$ in Water. *J. Mater. Chem. C* **2019**, 7, 15057–15065.

[19] Wang, X.; Feng, D.; Tang, J.; Zhao, Y.; Li, J.; Yang, J.; Kim, C. K.; Su, F. A Water-Stable Zinc(II)-Organic

Framework as a Multiresponsive Luminescent Sensor for Toxic Heavy Metal Cations, Oxyanions and Organochlorine Pesticides in Aqueous Solution. *Dalton Trans.* **2019**, 48, 16776–16785.

[20] Suryawanshi, S. B.; Mahajan, P. G.; Bhopate, D. P.; Kolekar, G. B.; Patil, S. R.; Bodake, A. J. Selective Recognition of $MnO_4^-$ Ion in Aqueous Solution Based on Fluorescence Enhancement by Surfactant Capped Naphthalene Nanoparticles: Application to Ultratrace Determination of $KMnO_4$ in Treated Drinking Water. *J. Photochem. Photobiol., A* **2016**, 329, 255–261.

[21] Ye, Z.; Weng, R.; Ma, Y.; Wang, F.; Liu, H.; Wei, L.; Xiao, L. Label-Free, Fingle-Particle, Colorimetric Detection of Permanganate by GNPs@Ag Core-Shell Nanoparticles with Dark-Field Optical Microscopy. *Anal. Chem.* **2018**, 90, 13044–13050.

[22] Liu, H.; Rong, J.; Shen, G.; Song, Y.; Gu, W.; Liu, X. A Fluorescent Probe for Sequential Sensing of $MnO_4^-$ and $Cr_2O_7^{2-}$ Ions in Aqueous Medium Based on a UCNs/TMB Nanosystem. *Dalton Trans.* **2019**, 48, 4168–4175.

[23] Ding, P.; Xin, X.; Zhao, L.; Xie, Z.; Zhang, Q.; Jiao, J.; Xu, G. On-Off-On Fluorescent Oligomer as a Chemosensor for the Detection of Manganese(VII), Sulfur(II) and Aldehydes Based on the Inner Filter Effect. *RSC Adv.* **2017**, 7, 3051–3058.

[24] Du, F.; Li, G.; Gong, X.; Zhonghui, G.; Shuang, S.; Xian, M.; Dong, C. Facile, Rapid Synthesis of N,P-Dual-Doped Carbon Dots as a Label-Free Multifunctional Nanosensor for Mn(VII) Detection, Temperature Sensing and Cellular Imaging. *Sens. Actuators, B : Chem.* **2018**, 277, 492–501.

[25] Liu, H.; Zhao, Y.; Huang, B.; Liu, H.; Zhang, P.; Gu, W.; Ma, T. Zn-Based Three-Dimensional Metal-Organic Framework for Selective Fluorescence Detection in Zwitterionic Ions. *Int. J. Mol. Sci.* **2025**, 26, 3566–3579.

[26] Chen, K.; Cao, J.; Shang, Y.-J.; Gu, J.-Y.; Ding, W.-Y.; Wang, K.-Y.; Zhao, J.-L. Stable Interpenetrated Zirconium-Based Metal-Organic Framework for the Fluorescence Detection of $MnO_4^-$. *Inorg. Chem.* **2025**, 64, 6648–6655.